Vegetable oil-based non-isocyanate urethane methacrylate resins for greener vat photopolymerization 3D printing

Sustainable Materials and Technologies 49 (2026) e02145

Contents lists available at ScienceDirect

Sustainable Materials and Technologies

journal homepage: www.elsevier.com/locate/susmat

# Vegetable oil-based non-isocyanate urethane methacrylate resins for greener vat photopolymerization 3D printing

Gabriel I. dos Santos [a], Caroline Gaglieri [a], Rafael T. Alarcon [b], Marco Sangermano [c], Gilbert Bannach [a,*]

[a] Universidade Estadual Paulista (UNESP), Faculdade de Ciências, Bauru 17033-260, SP, Brazil
[b] Instituto de Química, Universidade Federal de Mato Grosso do Sul (UFMS), Campo Grande, 79070-900, Brazil
[c] Politecnico di Torino, Dipartimento di Scienza Applicata e Tecnologia, Torino 10129, Italy

ARTICLE INFO

*Keywords:*
Non-isocyanate urethane
3D printing
Photopolymerization
Sustainable photocurable resins
Renewable polymers

ABSTRACT

The development of sustainable photopolymer resins is essential to mitigate the environmental impact of additive manufacturing technologies. Herein, we report, for the first time, the application of a high-performance non-isocyanate urethane methacrylate (NIUMA) monomer, derived from passion fruit seed oil and carbon dioxide, in vat photopolymerization 3D printing. The synthetic route to NIUMA provides a safer alternative to conventional isocyanate-based systems while enabling a bio-based carbon content of 72%. Photocurable formulations incorporating 2-hydroxyethyl methacrylate, also explored here for the first time in combination with NIUMA, exhibited high monomer conversion (>95%), tunable viscosities (21-930 mPa·s), low critical exposure energies (2.58-4.05 mJ $cm^{-2}$), low volume shrinkage, and excellent printing resolution without the need for photoblockers. Sustainable formulation scores (SFS) reached up to 38, with NIUMA75 representing the first non-isocyanate urethane-based resin for vat photopolymerization to surpass an SFS of 30. The resulting 3D-printed materials display a unique combination of properties, including tunable thermomechanical behavior ($T_g$ = 72-104 °C), shape memory, aggregation-induced luminescence, and alkaline degradability. Notably, this work provides the first evidence of dynamic polymer network (DPN) behavior in NIUMA-based materials, enabling reprocessability and self-healing. By integrating biomass valorization, $CO_2$ utilization, circular material design, and advanced manufacturing, this study establishes a platform for sustainable, high-resolution photopolymer resins and expands the potential of NIUMA systems toward smart and functional 3D-printed materials.

## 1. Introduction

Polymers are ubiquitous and essential in our daily lives. They can be used across all industrial sectors, from simple household utensils to complex machinery and biomaterials [1–4]. A wide range of polymers is used for these purposes, including polyesters, polycarbonates, polyamides, polypropylene, polyethylene, polystyrene, polyacrylates, and polyurethanes [5,6].

The last two previously mentioned possess broad applicability owing to the ease of their polymerization and their outstanding physicochemical properties [7]. The global production of polyurethane is estimated at 26 million tons in 2023, primarily composed of isocyanates and polyol monomers [8]. In addition to their non-reprocessability and sometimes non-recyclability, the use of isocyanates raises concerns due to their harmful effects. Furthermore, the isocyanate presents low chemical stability, reacting rapidly with nucleophiles (e.g., alcohols, thiols, amines, epoxides, and water) to form the final product, which can cause two major problems: non-reaction control in some cases, and greater caution during storage [9–11].

To resolve this issue, cyclic carbonates can be used as replacements for isocyanates. Cyclic carbonates can react with amines to produce non-isocyanate poly(hydroxyurethanes) (NIPUs) [12,13]. The cyclic carbonate is usually synthesized by reacting epoxy compounds with $CO_2$ in a reactor under moderate conditions, using a co-catalyst (tetrabutylammonium bromide, TBAB) and a catalyst such as the greener bimetallic aluminum(salen) complex [13–16]. Since atmospheric $CO_2$ has increased due to anthropogenic activities (37,000 megatons per year), its use for the synthesis of cyclic carbonate monomers is consistent with

* Corresponding author at: Av. Eng. Luiz Edmundo C. Coube 14-01 - Núcleo Habitacional Presidente Geisel, Bauru SP/SP - CEP 17033-360, Brazil.
*E-mail addresses:* gabriel.i.santos@unesp.br (G.I. dos Santos), caroline.gaglieri@unesp.br (C. Gaglieri), rafael.alarcon@ufms.br (R.T. Alarcon), marco.sangermano@polito.it (M. Sangermano), gilbert.bannach@unesp.br (G. Bannach).

https://doi.org/10.1016/j.susmat.2026.e02145
Received 30 March 2026; Received in revised form 30 June 2026; Accepted 30 June 2026
Available online 1 July 2026

the carbon dioxide utilization (CDU) methodology [17,18]. Furthermore, this reaction exhibits 100% atom efficiency, which also aligns with the principles of Green Chemistry Principle 2) [13,19].

By adopting green design principles, including those of green chemistry, the circular economy, and the United Nations Sustainable Development Goals (UNSDGs), the synthesized monomers and polymeric materials should be made as sustainable as possible [20–22]. Considering the renewability of precursors, the synthetic route, solvent use, application, and final disposal - degradability [23–25]. In this context, lipid biomass is a promising feedstock for this purpose, particularly vegetable oil (VO; triacylglycerol), which contains alkenes that can be epoxidized and subsequently carbonated [26]. Moreover, its structure contains ester groups (in the glycerol backbone) that are susceptible to hydrolytic degradation in alkaline media (Principle 10) [19,26].

Therefore, passion fruit oil (PFO) was selected in this study. PFO is extracted from passion fruit seed, which is a waste of the juice and food industry [27,28]. This oil aligns with the 2° sustainable point (biomass from industrial waste) when the renewable precursor was selected [13,26]. The acrylated passion fruit seed oil has already been used as a sustainable monomer for 3D printing [28]. It can be epoxidized using a sustainable procedure that employs mild conditions (3 h at 60 °C), hydrogen peroxide, and acetic acid, thereby generating peracetic acid in situ in the presence of a heterogeneous catalyst (Amberlite IR120) and without solvent (Prilezhaev reaction) [28–30]. This reaction achieves epoxy conversions surpassing 95% and was developed with the aim of promoting the use of less hazardous chemicals (principle 3), energy efficiency (principle 6), a promising catalyst (principle 9), and accident prevention (principle 12) [19,26,29].

Subsequently, the epoxidized vegetable oil was used to produce carbonate vegetable oils, as previously mentioned. Carbonated vegetable oils typically react with polyamines to form NIPUs, which requires heating and 24 h for complete cure [31]. However, NIPUs have the advantage of containing non-reacted hydroxyl groups in their polymer structure; these groups are readily reactive with ester and urethane groups via thermal heating or under red light, enabling healing of the polymer after it has been powdered, shattered, or fractured [13,31–37]. This behavior is typical of dynamic polymer networks (DPNs), a class of smart materials that can exhibit, in addition to regeneration/healing, shape memory behavior. DPN materials are consistent with the principles of the circular economy, such as recycling and recovery [32,38–40].

Given the logical sequence for producing a new monomer, carbonated vegetable oil can be reacted with monoamine, such as ethanolamine, to yield a monomer with more hydroxyl groups, which can be called a hydroxyurethane monomer. Thereafter, the hydroxyl groups can easily react with methacrylic anhydrides to form the non-isocyanate urethane methacrylate (NIUMA) monomer.

The NIUMA contains methacrylic pendants that can be polymerized under light in the presence of a photoinitiator. Photopolymerization is aligned with energy efficiency (Principle 6) and is widely used in additive manufacturing (3D printing), including digital light processing (DLP), stereolithography (SLA), and continuous liquid interface production (CLIP) [41,42]. The photopolymerization and additive manufacturing market was valued at approximately $1.38 billion in 2025 and is projected to reach $5.56 billion by 2035 [43]. 3D printing via photopolymerization (also known as vat photopolymerization) offers a significant advantage in fabricating intricate structures with high resolution, owing to its layer-by-layer polymerization process, controlled thickness, and exposure duration [44–48].

NIUMA has been reported in the literature to provide more sustainable polymers for various applications. Liu et al. [49] reported in 2025 a UV-curable NIUMA derived from sorbitol cyclic carbonate and monoamines (without hydroxyl groups) for use as anti-smudge and anti-graffiti coatings. Singh, Bakhshi, and Meyer [50] have synthesized a series of new linear NIUMAs using ethylene carbonate (EC) and propylene carbonate (PC) as precursors; these monomers were then used in 3D printing (photopolymerization) to obtain flexible structures. Carmenini et al. [51] also reported the reaction of EC and PC with 1,4-diaminobutane, which was further reacted with monomethyl itaconoyl chloride, providing linear itaconic non-isocyanate monomers for 3D printing. Liu et al. [52] also reported NIUMAs for 3D printing using 4,5-epoxycyclohexane-1,2-dimethyl dioxolane cyclic carbonate as a precursor, which was reacted with n-butylamine, *n*-hexylamine, benzylamine, and methacrylic anhydride; these monomers were used in 3D printing, yielding structures with high resolution in a low light-exposure time (5 s). In 2024, Lam et al. [53] synthesized an NIUMA from carbonated palm olein (iodine value of 55 g $I_2$/100 g); the final polymer presented elastomeric properties.

These studies demonstrated the applicability of NIUMAs and advances in polymer science and 3D printing, highlighting a promising area for future investigation. In this context, the present work aims to develop a new renewable NIUMA formulation using carbonated passion fruit oil as the primary component (Principle 7). The synthetic route was designed to produce an intermediate containing additional hydroxyl groups. Then, the carbonated compound reacted with ethanolamine, and the resulting hydroxyurethane was subsequently reacted with methacrylic anhydride. The developed NIUMA is suitable for 3D printing when reactive diluents are employed (e.g., 2-hydroxyethyl methacrylate - HEMA). Besides the production of polymers with high-resolution printing, luminescence, and hydrolysis in an alkaline solution, the synthetic approach introduced urethane and ester groups into the monomer structure, which produced a material with DPN behavior. These characteristics are consistent with principles of green chemistry, the United Nations Sustainable Development Goals (UNSDGs), and the circular economy, thereby substantiating the environmentally sustainable design presented in this study. To the best of our knowledge, this is the first time that photocurable resins based on a non-isocyanate urethane methacrylate monomer derived from vegetable oil have been applied in vat photopolymerization 3D printing for producing smart materials with shape-memory, luminescence, and DPN behavior.

## 2. Experimental

### 2.1. Materials

Passion fruit oil-PFO (batch code: 0005/22-A) was purchased from Mundo dos Óleos (Brasília, Brazil). Hydrogen peroxide ($H_2O_2$; 50%), glacial acetic acid (≥ 99%), Amberlite IR-120, tetrabutylammonium bromide (TBAB; 99%), methacrylic anhydride (MA; ≥99%), *p*-Toluenesulfonic acid (*p*-TSA; 98.5%), hydroquinone (≥ 99%), ethyl acetate (≥ 99%), (2-hydroxyethyl methacrylate (HEMA; 99%), diphenyl(2,4,6-trimethylbenzoyl)phosphine oxide(TPO; 97%), ethanolamine (98%), dibutyltin dilaurate (DBTDL; 95%), and deuterated chloroform ($CDCl_3$; 99.8%) were acquired from Sigma-Aldrich and utilized without purification. The non-biobased and commercial resin RP-405 was purchased from 3DFila.

### 2.2. Modification of passion fruit oil

PFO was subjected to $^1$H NMR analysis to determine the iodine value (IV), which was further converted to moles of carbon double bonds (C=C) [29]. Then, the epoxidation of PFO was performed according to the previously used procedure, resulting in the epoxidized passion fruit oil (EPFO; yield: 98%) [28].

Subsequently, EPFO was carbonated following the literature route [54]. Thus, the epoxidized vegetable oil (150 g) was inserted into a reactor under 10 bar of $CO_2$ and left to react under stirring at 100 °C for 24 h. Additionally, a combination of TBAB and a bimetallic aluminum (salen) complex was used as the catalyst system [54]. After purification, a brown, viscous liquid was obtained and designated as carbonated passion fruit oil (CPFO; yield: 99%).

Non-isocyanate urethane (NIU) from CPFO was obtained according

to a procedure described in the literature, with some adaptations [53]. Therefore, the carbonated vegetable oil reacted with ethanolamine in a stoichiometric proportion of carbonate and amine groups. The reaction was conducted for 2 h at 50 °C (yield: 99%).

The purified NIU was subjected to a methacrylation reaction in a similar way to that found in the literature [49]. Thus, the compound was reacted with methacrylic anhydride, respecting a stoichiometric molar ratio of 1:1 between the hydroxyl and methacrylic groups. 1.0 wt% of *p*-TSA was used as a catalyst, and 0.2 wt% of hydroquinone as the polymerization inhibitor (the percentage of each component was relative to the mass of MA). The reaction was conducted in continuous stirring for 6 h at 80 °C. The crude product was dissolved in ethyl acetate and washed several times with a saturated sodium bicarbonate solution to remove the excess of methacrylic acid, followed by distilled water. The organic phase was dried with anhydrous magnesium sulfate and then evaporated in a rotary evaporator at 50 °C to remove the solvent. The product, non-isocyanate urethane methacrylate, was allowed to rest for 24 h in a vacuum chamber to remove any traces of MA and was named NIUMA. Yield: 92%.

Fig. 1 shows all the synthetic steps for the preparation of NIUMA. PFO and all products obtained after each reaction were characterized by using MIR and $^{1}$H NMR. All reactions were performed without any solvent, and ethyl acetate was just used in the purification steps of EPFO, CPFO, NIU, and NIUMA syntheses, as this solvent is recommended by the CHEM21 selection guide of classical- and less classical solvents [55].

### 2.3. Formulation of NIUMA-based photocurable resins

All formulated resins were produced by mixing bio-based NIUMA with the potential bio-based reactive diluent HEMA in different weight proportions, which are shown in Table 1. Besides, the photoinitiator TPO was added to each formulation (3.0 wt% of the monomeric mixture weight). After adding all components, each resin was stirred continuously for 20 min at ambient temperature. After that, homogeneous solutions were observed. The scheme in Fig. 1 summarizes the resin formulation process.

### 2.4. Digital light processing (DLP) 3D printing using NIUMA-based resins

Suitable resins were applied in DLP 3D printing. The setup for the printing process was composed of an Elegoo Mars 2 Pro DLP 3D printer equipped with a 405 nm light source ($E_{max}$ = 3.8 mW cm$^{-2}$) and an Elegoo Wash & Cure Mercury Plus for the washing and post-curing process (405 nm). 3D objects for the printability study and material characterization were sliced, and printing parameters, such as exposure time and layer thickness, were adjusted using Chitubox software (Table 2). After printing, all objects and specimens were washed with isopropyl alcohol and post-cured for 30 min. All printing conditions were kept the same for all resins to investigate the thermal and chemical properties of the produced materials. The materials from NIUMA25, NIUMA50, and NIUMA75 were respectively named as PNIUMA25, PNIUMA50, and PNIUMA75.

### 2.5. Characterization

#### 2.5.1. Viscosity

Viscosity (η) analysis of HEMA, NIUMA25, NIUMA50, and NIUMA75 was acquired in a digital rotary viscosimeter, Brookfield DV-III rheometer (Brookfield, Toronto, Canada) equipped with a water bath. The analysis was conducted at 27 °C, and due to different viscosities observed in the sample, the following spindles were utilized: SC4-18 for HEMA, NIUMA25, and NIUMA50; SC4-34 for NIUMA75. NIUMAR was not analyzed because its viscosity is very high (exceeding the capacity of the equipment and the spindles' range).

#### 2.5.2. $^{1}$H-NMR analysis

$^{1}$H-NMR spectra were acquired in an Agilent 400 MHz Premium Shield spectrometer. PFO, EPFO, CPFO, NIU, and NIUMA were solubilized in deuterated chloroform ($CDCl_3$, 99.8% D, Sigma-Aldrich) with TMS as the internal reference. The $^{1}$H-NMR analysis was used to determine the iodine value (*IV*) of PFO and to verify the incorporation of new functional groups and the extent of conversion after each reaction.

The *IV* was determined using eq. (1) [29], where *K* is the integration value of the vinyl hydrogens multiplet at 5.34 ppm when the spectrum is

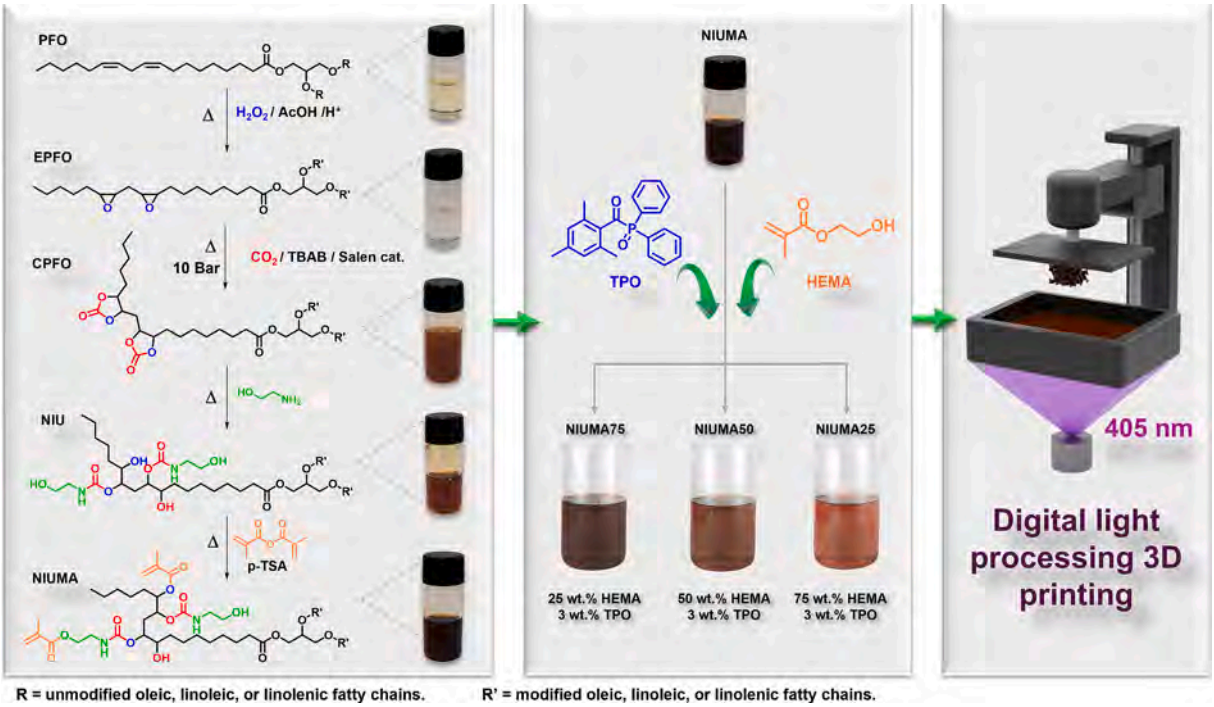


**Fig. 1.** Scheme of synthetic approaches used in this work, resin formulation, and application of the resins in a digital light processing 3D printer.

**Table 1**
Composition of each photocurable resin and the corresponding photoinitiator amount.

| Resin name | NIUMA (wt%) | HEMA (wt%) | TPO amount/wt%[a] |
|---|---|---|---|
| NIUMAR | 100 | 0 | 3.0 |
| NIUMA75 | 75 | 25 | 3.0 |
| NIUMA50 | 50 | 50 | 3.0 |
| NIUMA25 | 25 | 75 | 3.0 |

[a] The percentage of photoinitiator was calculated based on the total mass of monomers in the resin (NIUMA + HEMA).

normalized by the α-carbonyl hydrogens at 2.31 ppm (six hydrogens). Dividing the *IV* value by the molar mass of $I_2$ (253.808 g $mol^{-1}$), the mole number of alkenes in 100 g of oil was determined.

$$IV = \frac{(12691 \times K)}{(821.3 + 6.006 \times K)} \quad (1)$$

After the methacrylation reaction, the average methacrylate groups (*MAG*) attached to a triacylglycerol molecule were determined according to eq. (2), in which *MAH* is the total area of the vinyl hydrogens between 5.54 and 6.14 ppm, and *αH* is the α-carbonyl hydrogens in the acyl chain (at 2.31 ppm).

$$MAG = \frac{MAH}{\left(\frac{\alpha H}{6}\right)} \quad (2)$$

### 2.5.3. Mid-infrared spectroscopy (MIR)

MIR analysis was conducted in order to verify the incorporation of functional groups into the triacylglycerol structure and the conversion of monomer to polymer. The spectra were acquired in a Bruker Vertex 70 FTIR spectrometer with an attenuated total reflectance diamond crystal accessory. The following settings for the measurements were: a range of 4000 - 400 $cm^{-1}$ with 32 scans and 4 $cm^{-1}$ of resolution.

The monomer conversion to polymer (*MC*) during the photopolymerization reaction was investigated as previously reported in the literature [28,56]. Thus, after NIUMA and each formulated resin was spread onto the diamond window of the same equipment reported above, each sample was irradiated with an ultraviolet lamp (370 nm, Kessil KSPR160, $E_{max}$ = 399 mW $cm^{-2}$) for 120 s with a distance of 2 mm between the lamp and the resin surface. Spectra were then collected every 10 s until the final time (conditions: range of 4000 - 400 $cm^{-1}$ with 1 scan and 4 $cm^{-1}$ of resolution), and the progress of the photopolymerization reaction was investigated by monitoring the area of the band of the C═C from the methacrylic groups at 1637 $cm^{-1}$ ($A_{1637}$). All spectra were normalized by the area of the C—H stretching band of the methylene groups at 2854 $cm^{-1}$ ($A_{2854}$). Finally, the *MC* values were calculated using eq. (3), considering the moment before UV exposure ($t = 0$) and the corresponding UV exposure time ($t = x$). All samples were analyzed in triplicate.

$$MC\ (\%) = \frac{(A_{1637}/A_{2854})_{t=0} - (A_{1637}/A_{2854})_{t=x}}{(A_{1637}/A_{2854})_{t=0}} \times 100 \quad (3)$$

The rate of polymerization ($R_p$, $s^{-1}$) was calculated according to eq. (4), where $\Delta_A$ is the difference between the two areas of the band from the C═C bond on the methacrylic groups at 1637 $cm^{-1}$, $A_0$ is the initial area of the C═C band (before the UV exposure), and $\Delta_t$ is the time difference between each analysis [56,57].

$$R_p = \left(\frac{\Delta_A}{A_0 \times \Delta_t}\right) \quad (4)$$

A similar approach was used to determine the carbonate conversion (*CC*) by MIR analysis to study the progress of the acyl nucleophilic substitution reaction with ethanolamine [54]. Thus, the area of the C═O band from the carbonate ring at 1793 $cm^{-1}$ was monitored at different times (0, 10, 20, 30, 60, and 120 min), and the percentage of *CC* was determined according to eq. (5). All spectra were normalized to the area of the C—H band at 2854 $cm^{-1}$, and the same equipment mentioned above was utilized.

$$CC\ (\%) = \frac{(A_{1793}/A_{2854})_{t=0} - (A_{1793}/A_{2854})_{t=x}}{(A_{1793}/A_{2854})_{t=0}} \times 100 \quad (5)$$

### 2.5.4. Differential scanning calorimetry (DSC) and photo-DSC

The DSC curves for each material were obtained in a DSC1 Star[e] equipment (Mettler Toledo). The analyses were conducted using 5 mg of the sample, weighed in a 40 μL aluminum crucible with a perforated lid. The curves were recorded in a temperature range of -30 to 150 °C, with a heating rate of 10 °C $min^{-1}$, under an air flow rate of 50 mL $min^{-1}$.

The photo-DSC analyses were performed on the same equipment in isothermal mode at 25 °C and with an air flow rate of 50 mL $min^{-1}$. Then, approximately 5 mg of each formulated resin was weighed into an open aluminum crucible and cured with a UV lamp Kessil KSPR160 (370 nm) at an intensity of 100% ($E_{max}$ = 399 mW $cm^{-2}$) for 120 s. To determine exactly the exothermic event caused by photopolymerization, two isothermal cycles were conducted under the same conditions, and the second curve was subtracted from the first. Finally, the percentage of monomer to polymer conversion (*C*) for each formulation was calculated according to eq. (6), in which $\Delta H_{total}$ is the theoretical enthalpy for a complete methacrylic double bond conversion, and *dH/dt* is the heat flow under an isothermal condition ($T$ = 25 °C) [58,59].

$$C = \left[\frac{1}{\Delta_{total}} \times \int_t^0 \left(\frac{dH}{dt}\right) T\right] \times 100 \quad (6)$$

The rate of polymerization ($R_p$, $s^{-1}$), which is directly related to the heat flow (*dH/dt*) by eq. (7), was determined [60].

$$R_p = \frac{1}{\Delta_{total}} \times \left(\frac{dH}{dt}\right)_T \quad (7)$$

The total enthalpy ($\Delta H_T$) of photopolymerization and the time at which the reaction reached maximum heat release (peak time, *PT*) were also determined.

### 2.5.5. UV–Vis analysis and photolysis study

Liquid UV–Vis analysis was conducted for PFO, EPFO, CPFO, NIU, and NIUMA in a Cary 8854 spectrophotometer (Agilent Technologies), at room temperature and using a Quartz cuvette with 1 cm of optical path. A solution of 1.0 mg $mL^{-1}$ for each sample was prepared in ethyl acetate. The photolysis study was conducted with the NIUMA solution by collecting spectra at different times of UV exposure (10, 30, 60, 180, and 300 s).

### 2.5.6. Simultaneous thermogravimetry–differential thermal analysis (TG – DTA)

TG-DTA curves were acquired in a STA 449 F3 equipment (Netzsch) using approximately 10 mg of sample, weighed in a 200 μL α-alumina crucible. The samples were submitted to a temperature ramp of 30 to 800 °C at 10 °C $min^{-1}$, in a dry air atmosphere with a flow rate of 70 mL $min^{-1}$.

### 2.5.7. Bio-based carbon content

The bio-based carbon content (*BCC*) was determined from eq. (8) for each formulation component [61], considering the vegetable oil core and ethylene glycol moiety of HEMA as renewable sources of carbon ($C_{renewable}$). Meanwhile, the methacrylic and urethane moieties in NIUMA, the methacrylic moiety in HEMA, as well as the photoinitiator TPO, were considered non-renewable ($C_{non\text{-}renewable}$).

$$BCC(\%) = \left(\frac{C_{renewable}}{C_{renewable} + C_{non-renewable}}\right) \quad (8)$$

From the *BCC* value of each compound used in the resin formulation,

**Table 2**
Printing parameters used to produce all designed objects/specimens from all resins.

| Printing parameters | Settings |
|---|---|
| Layer height | 0.05 mm |
| Base layer amount | 20 |
| Exposition time for base layers | 50 s |
| Exposition time for the rest of the layers | 15 s |
| Elevation after printing | 5 mm |

the bio-based carbon content of the formulation (*BCCF*) was calculated following eq. (9) [61,62].

$$BCCF(\%) = (w_i \times BCC_{NIUMA}) + (w_i \times BCC_{HEMA}) \quad (9)$$

Where $w_i$ is the weight fraction of the compound in the resin.

### 2.5.8. Sustainable formulation score

The sustainable formulation score (*SFS*) was calculated according to eq. (10) [61]. It considers synthesis factors, hazardous reagent usage, solvent selection, and end-of-life considerations [61].

$$SFS = 100 \times F_{EoL} \times \sum_{i=1}^{n} \left(w_i \times BCC_i \times F_{syn,i}\right) \quad (10)$$

$F_{EoL}$ is the end-of-life factor, and $\sum_{i=1}^{n} \left(w_i \times BCC_i \times F_{syn,i}\right)$ is the weighted sum of biobased carbon content multiplied by the respective synthetic factors ($F_{syn}$) and weight fraction ($w_i$) of each component [61]. The $F_{syn}$ was determined according to eq. (11) for each resin component:

$$F_{syn} = f_{haz} \times f_{sol} \times f_{T+t} \times AE \quad (11)$$

where $f_{haz}$ is related to the use of hazardous chemicals in the synthesis of the respective compound, $f_{sol}$ contributes to the sustainability of the solvent, $f_{T+t}$ is a temperature-time factor of the synthesis, and *AE* is the atom economy defined by eq. (12) [61]:

$$AE = \frac{MW_i}{\sum_j (n_j \times MW_j)} \quad (12)$$

where $MW_i$ is the molecular weight of component *i* and $\sum_j \left(n_j \times MW_j\right)$ is the sum of the molecular weight multiplied by the respective number of equivalents of all reagents *j* used in the synthesis of 1 equivalent of component *i*.

### 2.5.9. Working curves

The working curves were used to assess the curing properties of the resins NIUMA25, NIUMA50, and NIUMA75 during the printing process, such as critical energy ($E_c$) and the penetration depth ($D_p$) [56,57,63]. Thus, on an Elegoo Mars 2 Pro DLP 3D printer (405 nm and constant intensity of 3.8 mW $cm^{-2}$), one-layer squares were cured, varying the exposure time (15-600 s) and at room temperature. After curing, each sample was washed with isopropyl alcohol, and its thickness was measured with a micrometer to obtain the curing depth ($C_d$), which was used to develop a semilogarithmic plot showing its dependence on the exposure energy of the incident light on the resin surface ($E_{max}$). The eq. (13), derived from the Beer-Lambert law, was used to determine $D_p$ (slope of the curve) and $E_c$ (x-axis intercept).

$$C_d = D_p ln(E_{max}/E_c) \quad (13)$$

### 2.5.10. Printing resolution analysis

A comb-shaped structure with walls and cavities of varying dimensions was designed and 3D-printed (using the same equipment and conditions described previously) to assess the printing resolution and overcuring behavior of the NIUMA25, NIUMA50, and NIUMA75 resins. The cavity radii and wall widths were measured with a digital calliper, yielding empirical values that were compared with the theoretical dimensions from the CAD model. The *%overcure* (%) was determined according to Eqns. (14) and (15) [57,64,65].

$$\%overcure_{cavity} = \frac{Theoretical - Empirical}{Theoretical} \quad (14)$$

$$\%overcure_{square} = \frac{Empirical - Theoretical}{Theoretical} \quad (15)$$

### 2.5.11. Optical microscopy

Surface images of the 3D-printed objects were captured with a Global Optics microscope.

### 2.5.12. Tensiometric analysis

The contact angle of each 3D-printed polymer was measured using a C201 Attension Theta Flex optical tensiometer controlled by the One Attension software (Biolin Scientific) and equipped with a Navitar digital camera. A droplet of deionized water was deposited on the surface of each polymer, and 50 optical images were recorded to determine the contact angle formed between the droplet and the polymer surface.

### 2.5.13. Dynamic mechanical analysis

The relaxation tests were performed in a Q800 instrument (TA Instruments). Samples with dimensions of 20 mm in length, 5 mm in width, and 1 mm in thickness were 3D-printed, post-cured (using the same conditions already reported in this work), and subsequently analyzed. The temperature range was set from -30 to 145 °C, with a heating rate of 3 °C $min^{-1}$ and a frequency of 1 Hz. The storage modulus ($E'$) and Tan δ curves were obtained. The glass transition temperature ($T_g$) was determined from the temperature at the peak of the α-transition in the Tan δ curve [66].

The crosslink density ($\nu$) of the materials was calculated using eq. (16) [66].

$$\nu = \frac{E'}{3RT} \quad (16)$$

Where *T* is the temperature in Kelvin in the rubbery region (Tan δ + 40 °C), $E'$ is the storage modulus in the rubbery region (determined at temperature *T*), and R is the gas constant (8.314 J $mol^{-1}$ $K^{-1}$). The tensile test was performed on the same equipment at 25 °C.

### 2.5.14. Gel content and hydrolysis test

The gel content (*GC*) values were obtained by submitting each polymer to Soxhlet extraction with ethyl acetate under reflux for 24 h. After this step, samples were dried in an oven at 80 °C for 3 h. The *GC* was calculated using eq. (17), in which $W_i$ is the initial weight of the polymers and $W_f$ is the final weight (after drying).

$$GC\ (\%) = \left(W_f / W_i\right) \times 100 \quad (17)$$

The hydrolysis test was performed by immersing all polymers in an acid solution (HCl, 1 mol $L^{-1}$) and in a basic solution (NaOH, 1 mol $L^{-1}$) for 48 h at room temperature. Pictures were recorded at different times (0, 3, 13, 24, and 48 h).

### 2.5.15. Hardness

The hardness of each material was evaluated using an analogical Shore D durometer. The specimens used were 3D-printed in the form of squares (30 mm length, 30 mm width, and 10 mm thickness).

### 2.5.16. Shape memory test

The qualitative shape memory test was performed using 3D-printed complex objects (hexagonal grid structures) produced from each resin (NIUMA25, NIUMA50, and NIUMA75). The test was subdivided into three steps. In the first step, the sample was heated to 20 °C above its respective glass transition temperature ($T_g$). In the second step, the sample was reshaped by an external force, and the temperature was

reduced to 0 °C while maintaining the applied force. In the third step, the external force was removed, and the temperature was increased to $T_g$ + 20 °C, and the recovery time was recorded while images were captured at different time intervals.

## 3. Results and discussion

### 3.1. MIR and $^1$H NMR analysis of the structural modifications

The MIR spectra for PFO and the products obtained after each reaction are shown in Fig. 2a, the bands of greatest interest were highlighted, as their variations indicate the occurrence of structural changes. Thus, the band at 3008 cm$^{-1}$ is assigned to vinyl C—H stretching, while the absorptions at 1744 cm$^{-1}$ and 1650 cm$^{-1}$ correspond to C═O stretching of ester groups in the triglyceride backbone and C═C stretching of alkenes in unsaturated fatty esters, respectively. Following epoxidation, the disappearance of the bands at 3008 and 1650 cm$^{-1}$ indicates the consumption of unsaturated bonds to produce oxiranes, as evidenced by the appearance of new bands at 843 and 824 cm$^{-1}$, attributed to C-O-C stretching on the epoxide ring [29].

In the spectrum of CPFO, it is possible to observe that the epoxide group band (843-824 cm$^{-1}$) disappeared completely, while new bands corresponding to C═O and C—O stretching from the five-membered carbonate ring of carbonate groups appeared at 1793 cm$^{-1}$ and 1049 cm$^{-1}$, respectively. These changes indicate that the carbonation reaction occurred [54].

The NIU synthesis was performed in the presence of ethanolamine, a bifunctional molecule containing both amine and hydroxyl groups. At this stage, the synthetic strategy is based on a nucleophilic acyl substitution reaction, in which the amine group attacks the carbonate ring of CPFO, leading to the formation of hydroxyurethane structures enriched in free hydroxyl groups for subsequent functionalization. This approach enables the production of NIU units while avoiding crosslinking between polymer chains via copolymerization, which typically results in solid materials and limits further synthetic modification. However, as previously reported in the literature [31,54,67], a competing reaction may occur, wherein the amine group attacks the carbonyl of the glyceridic moiety in the triacylglycerol structure (Fig. 2b). Therefore, the NIU synthesis reaction was monitored by collecting MIR spectra at different reaction times, as shown in Fig. 2c. A decrease in the C═O stretching bands at 1793 cm$^{-1}$ and 1744 cm$^{-1}$ (attributed to carbonates and triglycerides, respectively) was observed, confirming the occurrence of the formation of the secondary product. In addition, two new bands that increase in intensity as the reaction progresses are observed at 1695 cm$^{-1}$ and 1533 cm$^{-1}$, which are respectively associated with C═O stretching vibration and N—H bending of the formed carbamate groups [68].

The carbonate conversion was determined (Fig. 2d), resulting in a value of 64% after 10 min of reaction and reaching 92% after 120 min. Although the extent of the reaction involving glyceridic carbonyls was not determined (due to band overlap), it can be suggested that the fraction of the secondary product was significantly lower than that of the primary product (since ethanolamine was used in a stoichiometric amount relative to the carbonate groups). It should be emphasized that this represents a significant advance in carbonate-amine reactions for the production of non-isocyanate hydroxyurethanes, as similar conversions usually require reaction times longer than 24 h, a higher proportion of the reactants, and temperatures higher than those used in this work [53,54,68–70]. Therefore, this step agrees with Principles 2 and 6 of Green Chemistry (Atom economy and Design for energy efficiency) [19].

In addition to the aforementioned bands, the NIU MIR spectrum (Fig. 2a) shows a broad band corresponding to O—H stretching vibrations between 3670 and 3135 cm$^{-1}$, as well as an increase in band intensity at 1252 cm$^{-1}$ related to C—O stretching. These two bands suggest the presence of alcohol groups in the NIU structure [71]. These bands decrease, and a new C═C stretching band at 1637 cm$^{-1}$ (magnified in Fig. S1) appears after the methacrylation reaction, confirming the incorporation of these groups into the triglyceride structure, as observed in the NIUMA spectrum (Fig. 2a).

Prior to epoxidation, the PFO was characterized by $^1$H NMR to determine the moles of alkenes per 100 g of oil, which is obtained from iodine value (*IV*). The vegetable oil presented an *IV* of 128.3 g of $I_2$ per 100 g of sample, which corresponds to 0.5067 mol of alkenes. This quantification was important to determine the conditions of epoxidation.

The $^1$H NMR spectra collected at the end of each reaction are shown in Fig. 3, with the signals of interest highlighted. Full range $^1$H NMR spectra are provided in the SI (Fig. S2-S6). After the epoxidation, the

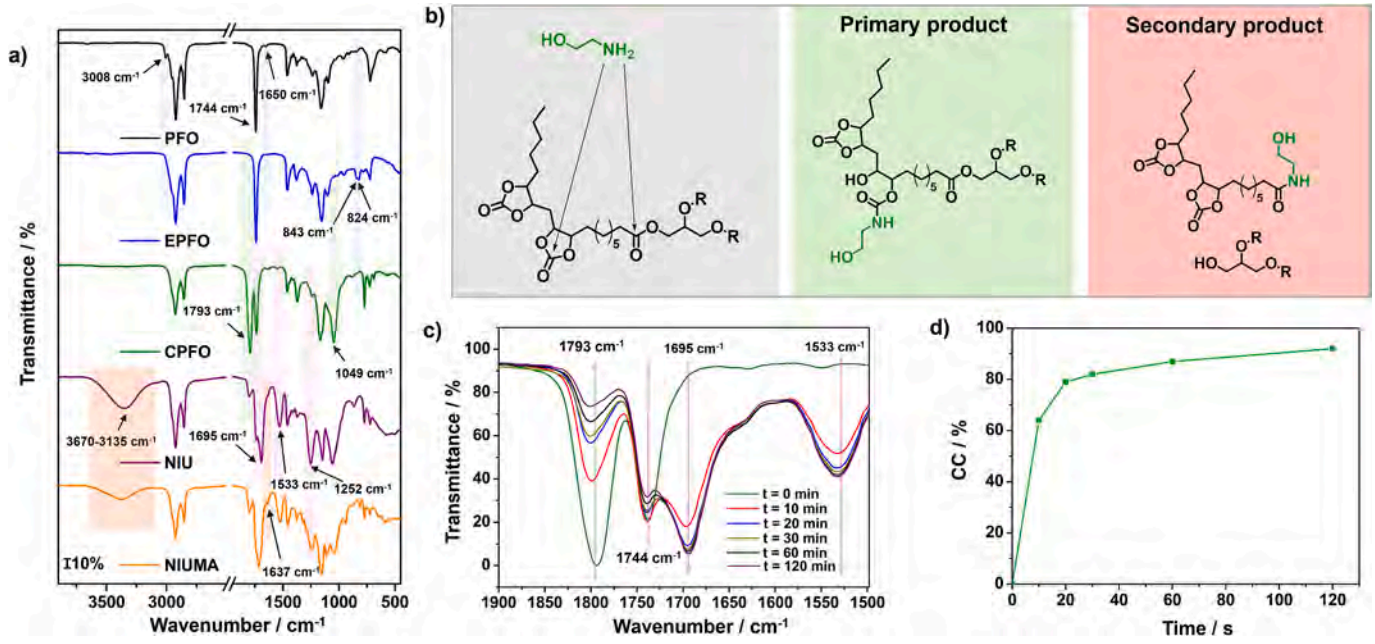


**Fig. 2.** a) MIR spectra of PFO, EPFO, CPFO, NIU, and NIUMA, b) possible reactions between amine and acyl groups of CPFO, c) magnified MIR spectra of the reaction progress for NIU production, and d) carbonate conversion over time.

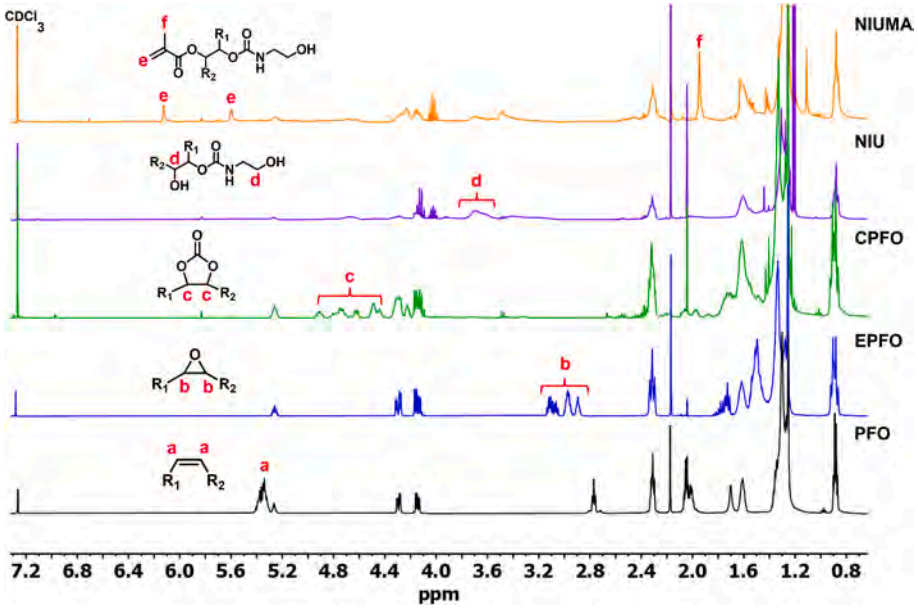


**Fig. 3.** $^{1}$H NMR spectra for a) PFO, b) EPFO, c) CPFO, d) NIU, and e) NIUMA.

multiplet at a chemical shift of 5.34 ppm, attributed to the vinylic protons of PFO, disappeared, and new signals between 3.16 and 2.85 ppm, corresponding to protons of the epoxide rings, were observed [29]. Following the carbonation step, the signals of hydrogens attached to the epoxide ring disappeared, and new protons from five-membered cyclic carbonates appeared at 4.22, 4.48, 4.61, 4.75, and 4.90 ppm [54], disappearing after reaction with ethanolamine. NIU presented a new signal between 3.53 and 3.79 ppm (protons d), which is attributed to the methylene protons adjacent to the hydroxyl groups [51,53,72,73]. Additional overlapping signals appeared in the region between 4.22 and 4.95 ppm, which may arise from protons bonded to carbons adjacent to ester or amide from urethane groups [49,72] as shown in Fig. S7.

Finally, after the methacrylation reaction, a marked decrease in the intensity of the signal corresponding to protons d was observed, confirming the incorporation of methacrylate groups in NIUMA. Moreover, two new singlets at chemical shifts of 5.60 and 6.13 ppm appeared, which are assigned to the vinylic protons of the methacrylate moieties. A singlet at 1.63 ppm, attributed to the methyl protons of the methacrylate group, was also observed. Thus, along with MIR data, these features confirm the formation of NIUMA.

These changes in $^{1}$H NMR spectra demonstrate that the reactions proceeded successfully, achieving conversions of 99.8% for epoxidation, 99.1% for carbonation, and 68% for methacrylation. These conversions were respectively calculated from the integrals of the signals corresponding to vinylic protons, epoxide-ring protons, and methylene protons adjacent to the hydroxyl groups. All spectra were normalized using the six α-carbonyl protons at 2.31 ppm. The conversion of the NIU formation reaction was not determined by $^{1}$H NMR due to signal overlap (evaluated by MIR). The low conversion observed in NIUMA production is associated with the presence of both primary and secondary alcohols in the NIU structure. While primary alcohols are more susceptible to nucleophilic attack on the anhydride carbonyl, the secondary alcohols generated after cyclic carbonate ring opening are less reactive due to the steric hindrance effect and may require longer reaction times to become functionalized. [74,75]

Besides, according to eq. (2), the *MAG* was determined for NIUMA, resulting in a value of 2.55, which is similar to other methacrylate and acrylated vegetable oils used in vat photopolymerization 3D printing processes [28,56,76,77].

The high conversion values obtained in the epoxidation and carbonation steps are consistent with Principle 2 of Green Chemistry (atom economy) [19] and also contribute to achieving Sustainable Development Goals (SDGs) 12 and 13 of the United Nations (due to the consumption of $CO_2$ during the carbonation stage) [78].

### 3.2. Bio-based carbon content (BCC), bio-based carbon content of the formulation (BCCF), and sustainable formulation score (SFS)

We determined the *BCC* value for NIUMA and HEMA as 72% and 33%, respectively. The high value presented by NIUMA is attributed to the high number of bio-based carbons in the triglyceride chains. Although HEMA exhibited the lowest *BCC*, the carbon atoms originating from the ethylene glycol moiety [79] were considered bio-based, since ethylene glycol is already produced commercially from renewable feedstocks. Industrial routes include processes based on corn starch-derived sorbitol or sugarcane-derived ethanol, as implemented by companies such as Global Biochem, India Glycols Limited, and Greencol Taiwan Corporation [80].

The *BCCF* for each resin was determined according to eq. (9). As it is possible to verify in Table 3, the addition of HEMA to the formulation decreases the *BCCF* values as expected since HEMA has a lower *BCC* than NIUMA. However, all resins demonstrated bio-based carbon contents above 40%, making them recognized as green products, since a value above 25% is recommended to characterize a product as bio-based [81–83].

Maturi et al. [61] developed a metric that goes beyond the renewable content in the formulation and assesses the full sustainable profile of the overall formulation. This metric, termed the Sustainable Formulation Score (*SFS*), evaluates the sustainability of photocurable formulations for vat photopolymerization 3D printing by considering multiple parameters, including bio-based carbon content, atom economy, synthesis conditions, and end-of-life aspects. Thus, the *SFS* for all resins produced in this work was determined, initially calculating the synthetic factor for NIUMA and HEMA ($F_{syn}$), which resulted in a $F_{syn}$ of 0.66 and 0.59, respectively. This variable accounts for several attributes of the synthetic route, such as the use of hazardous substances, solvent consumption, temperature-time requirements, end-of-life considerations, and atom economy (*AE*) [61]. Except for AE, the other variables have predefined values according to synthetic conditions [61]. Therefore, using eq. (12), AE values of 0.92 and 0.88 were obtained for the production of NIUMA and HEMA, respectively.

The resulting *SFS* values are exhibited in Table 3, and each subfactor

**Table 3**
BCCF, SFS, and sustainability characteristics for the resins formulated.

| Resin name | BCCF (%) | SFS | Sustainability[61] |
|---|---|---|---|
| NIUMAR | 72 | 38 | Moderate |
| NIUMA75 | 62 | 32 | Moderate |
| NIUMA50 | 52 | 27 | Low |
| NIUMA25 | 43 | 21 | Low |

value for the calculation is provided in Table S1. The highest *SFS* is observed for NIUMAR, due to the absence of HEMA in the formulation, which classifies it as having moderate sustainability. When the reactive diluent is added to the formulation, the *SFS* decreases, leading to resins with low sustainability characteristics, except for NIUMA75. This resin presented an *SFS* equal to 32 and was therefore classified as having moderate sustainability. This characteristic of NIUMAR and NIUMA75 emerges from the integration of bio-based feedstocks, free-solvent syntheses, and the absence or low content of reactive diluent. So far, NIUMA75 is the first non-isocyanate urethane-based resin for vat photopolymerization 3D printing with an *SFS* above 30 [61]. Moreover, the *SFS* values of all NIUMA-derived resins could be further improved by using reactive diluents with higher bio-based carbon contents.

### 3.3. Viscosity, UV–vis, and photolysis study

Viscosity is an important parameter in vat photopolymerization 3D printing, as it can affect not only the photocuring process but also printing resolution and printing time. During DLP 3D printing, the build platform is elevated by a predetermined distance after each layer is cured. When this occurs, the resin must rapidly refill the resulting void, enabling rapid manufacturing and preventing resin depletion in the printing area. In addition, the resin must flow out of the internal features of the 3D-printed object during the process, thereby avoiding the curing of undesired excess resin. Consequently, it has been reported that resins with viscosities below 1300 mPa·s are suitable for commercially available DLP 3D printers [84–86]. In this work, different contents of HEMA were used as a low-viscosity (5.4 ± 0.04 mPa·s; Fig. 4a) reactive diluent, since the viscosity of NIUMA is very high due to the high number of possible H-bonding interactions in its structure (as shown in Fig. 4b).

Due to the Newtonian fluid behavior, the viscosities in this work were determined from the slope of the shear stress versus shear rate curves for each sample (Fig. S8). Therefore, as can be seen in Table 4, when HEMA content increased from 25 wt% to 75 wt%, the viscosity of NIUMA-based resins reduced from 930 ± 1 mPa·s to 21 ± 0.1 mPa·s. Hence, except for NIUMAR, all resins are feasible for DLP 3D printing at room temperature.

The UV–Vis absorption spectra of PFO, EPFO, CPFO, NIU, and NIUMA were investigated (Fig. 4c). Prior to any structural modification, PFO exhibits absorption bands at 269 and 280 nm, corresponding to π → π* transitions of C═C bonds in unsaturated ester chains, which disappear after the epoxidation reaction, as evidenced in the EPFO spectrum. After carbonation, a new band at 331 nm is observed in CPFO. This band originates from the n → π* transition of C═O bonds in the cyclic carbonate, which are conjugated with two atoms bearing nonbonding electron pairs (oxygen atoms).

Upon opening of the five-membered ring via amine attack, this conjugation is partially reduced, leading to a slight hypsochromic shift of the C═O n → π* transition band ($\lambda_{max}$ = 327 nm) in NIU. Finally, in the NIUMA spectrum, a shoulder at 286 nm is observed, which can be attributed to π → π* transitions of C═C bonds in the incorporated methacrylic moiety. Moreover, the bathochromic shift of the C═O n → π* transition band to 339 nm indicates an increase in conjugation following the incorporation of methacrylic groups into the triglyceride chain.

When irradiated at lower wavelengths, certain acrylated and methacrylated monomers can undergo self-initiated polymerization [87]. Thus, NIUMA was submitted to a photolysis study. As can be seen in Fig. 4d, after UV light (370 nm) exposure, the bands at 286 and 339 nm presented a decrease in their intensity with the increase in time of exposure. This result may arise from the consumption of double bonds and carbonyl groups to initiate the polymerization. Therefore, it is suggested that the high number of chromophore groups in NIUMA allows for strong absorption, leading to cleavage of the π bond of C═C and C═O or the abstraction of hydrogen due to triplet-state excitation, as shown in Fig. 4e [87–90]. It leads to radical formation, which further initiates the reaction of polymerization. This possible characteristic of

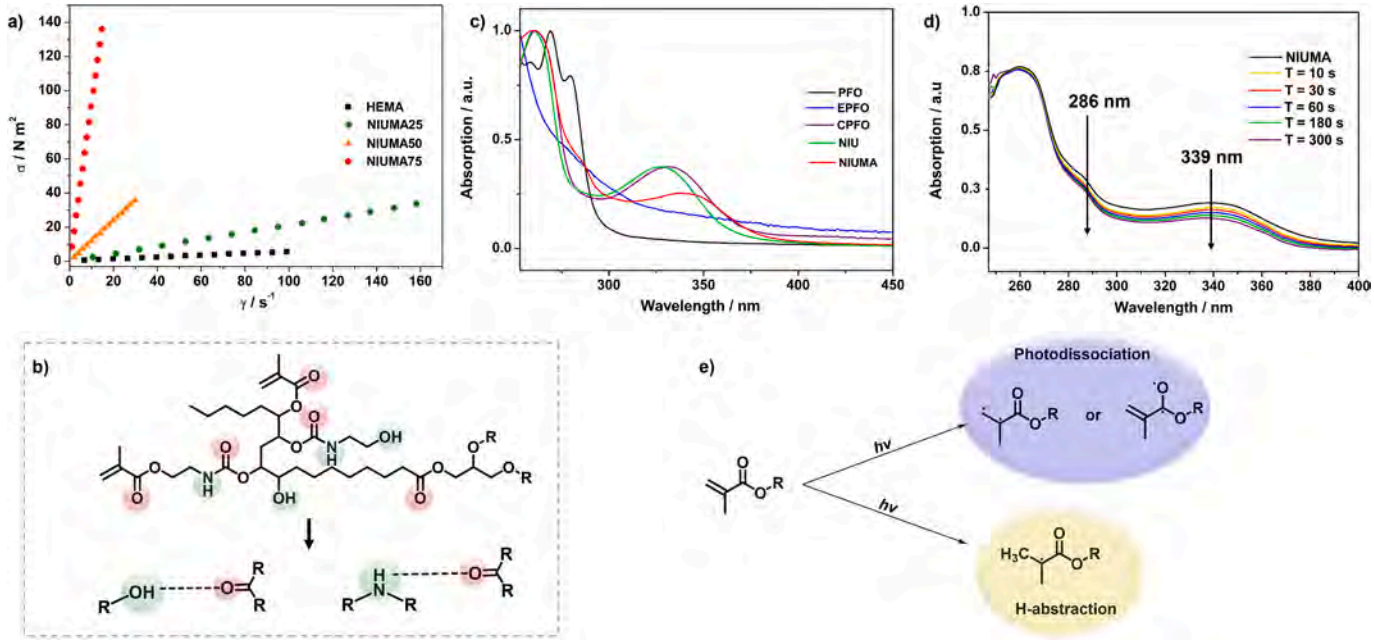


**Fig. 4.** a) Curves of shear stress vs. shear rate for HEMA and the formulated resins, b) scheme for hydrogen bond formation in NIUMA, c) UV–Vis spectra for each product obtained before and after each PFO modification, d) absorption spectra for NIUMA at different times under UV exposition, and e) proposed reaction pathway for self-initiation of methacrylates in NIUMA.

**Table 4**
Viscosity. Monomer Conversion (*MC*) and Rate of Polymerization ($R_p$) from MIR results. Total Enthalpy ($\Delta H_T$), Peak Time (PT), Conversion (C), and Rate of Polymerization ($R_p$) from Photo-DSC results.

| Resin name | | MIR | | Photo-DSC | | | |
|---|---|---|---|---|---|---|---|
| | Viscosity (mPa·s) | *MC* (%)[b] | $R_p$ ($s^{-1}$)[c] | $\Delta H_T$ (J $g^{-1}$) | *PT* (s) | *C* (%)[b] | $R_p$ ($s^{-1}$)[d] |
| **NIUMAR** | ---[a] | 96.0 ± 0.7 | 0.016 ± 0.004 | 83.6 | 4 | 18 | 0.006 |
| **NIUMA25** | 21.0 ± 0.1 | 96.8 ± 0.9 | 0.083 ± 0.001 | 275.4 | 9 | 86 | 0.074 |
| **NIUMA50** | 119.2 ± 0.3 | 99.7 ± 0.3 | 0.086 ± 0.002 | 238.9 | 6 | 97 | 0.098 |
| **NIUMA75** | 929.6 ± 1.3 | 99.8 ± 0.1 | 0.054 ± 0.003 | 181.3 | 4 | 86 | 0.087 |

[a] Not possible to measure due to high viscosity.
[b] Conversion at 120 s.
[c] Rate of polymerization at 10 s.
[d] Rate of polymerization at peak time.

the NIUMA monomer was suggested to improve its reactivity during photopolymerization, as demonstrated further in this work.

### 3.4. UV-curing behavior of NIUMA-based resins

As the reactivity of resins is a crucial factor in vat photopolymerization 3D printing, this attribute was investigated for all formulated NIUMA-based resins using MIR and photo-DSC. As shown in Fig. 5a-d (MIR spectra), double-bond consumption is clearly observed in all systems, as the corresponding band disappears as UV exposure proceeds. Consequently, values of monomer conversion (*MC*) were calculated at different times, as shown in Fig. 5e. At 10 s, the NIUMAR resin presented the lowest *MC* value (16 ± 4%). Meanwhile, NIUMA75, NIUMA50, and NIUMA25 formulations presented *MC* values of 56 ± 3%, 88 ± 2%, and 83 ± 1%, respectively. After 120 s, all resins exhibited *MC* values above 95% (Table 4), with NIUMA50 and NIUMA75 presenting almost complete curing (99.7 ± 0.3% and 99.8 ± 0.1%, respectively). It is suggested that the high conversion observed with these resins may arise from the self-initiating capability of NIUMA, which can continuously generate radical species during photopolymerization. [90–92] In addition, the incomplete conversion of NIUMA25 can be attributed to the rapid decrease in chain mobility caused by the excess of HEMA, which reduces the diffusion of reactive species during the propagation step [93]. Except for NIUMAR, all resins demonstrated excellent reactivity, as they reached the maximum rate of

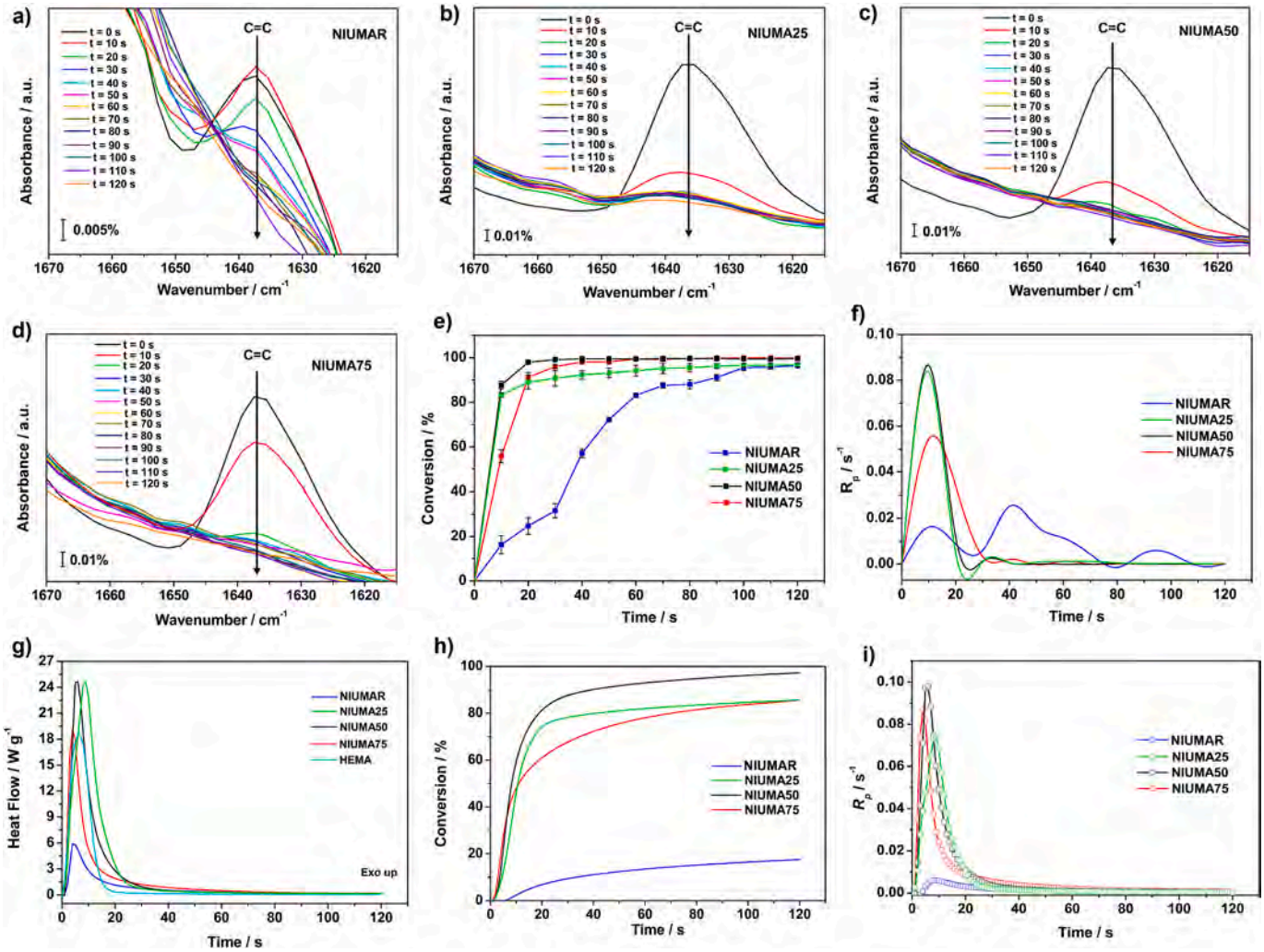


**Fig. 5.** Magnification of the MIR spectra highlighting the C═C band of a) NIUMAR, b) NIUMA25, c) NIUMA50, d) NIUMA75 resins during the photopolymerization. e) Monomer conversion versus time and f) rate of polymerization for each formulated resin obtained from MIR analysis. g) Heat release, h) monomer conversion, and i) rate of polymerization from photo-DSC results for each formulated resin.

polymerization ($R_p$) within 10 s, as shown in Fig. 5f and Table 4. In addition, the incorporation and variation of HEMA content significantly affected $R_p$. Accordingly, at 10 s, NIUMAR presented the lowest $R_p$ value ($0.016 \pm 0.004\ s^{-1}$), followed by NIUMA75 ($R_p = 0.054 \pm 0.003\ s^{-1}$), whereas NIUMA50 and NIUMA25 exhibited the highest $R_p$. For NIUMAR, the maximum $R_p$ was only observed after 40 s ($0.025 \pm 0.002\ s^{-1}$).

The slower polymerization of NIUMAR can be attributed to two main factors: viscosity and color. NIUMAR is a highly viscous compound with a dark brown color. When exposed to UV light, monomer mobility is restricted due to the high viscosity, leading to reduced radical diffusion and localized gelation at shorter irradiation times [94,95]. Additionally, the dark coloration of NIUMA, arising from its high content of chromophore groups that absorb at wavelengths overlapping with those of TPO (Fig. S9), causes attenuation of the incident light via the inner filter effect. As a consequence, radical generation is reduced in the deeper regions of the resin layer, leading to slower polymerization [96,97].

From photo-DSC curves (Fig. 5g), the total enthalpy ($\Delta H_T$) and peak time ($PT$) were determined as shown in Table 4. As expected, NIUMAR presented the lowest $\Delta H_T$ (83.6 J $g^{-1}$). Meanwhile, HEMA presented a $\Delta H_T = 150.9$ J $g^{-1}$, and increasing its content in the formulated resins from 25 wt% to 75 wt%, the $\Delta H_T$ values increased from 181.3 to 275.4 J $g^{-1}$. Therefore, it can be clearly observed that the addition of HEMA mitigated the negative effects on NIUMA reactivity associated with its viscosity and color. Although HEMA acted effectively as a reactive diluent, increasing its content led to a higher $PT$. For example, the NIUMA25 resin reached the peak at approximately 9 s, whereas NIUMA75 reached it after 4 s, indicating a slightly slower photopolymerization when HEMA content was higher. These results suggest that, when the viscosity and color do not significantly impact the reactivity, the possible self-initiation capability of NIUMA promotes faster photopolymerization, as it enhances radical generation alongside the photoinitiator and accelerates the initiation stage of the reaction.

Using the $\Delta H_T$ values and eq. (6) and (7), the monomer conversion ($C$) and the rate of polymerization ($R_p$) were determined for each formulated resin, as shown in Fig. 5h and i. While NIUMAR exhibited the lowest $C$ and $R_p$ values, the resins containing the reactive diluent showed conversion levels above 86%. Furthermore, in contrast to the MIR results, NIUMA75 exhibited a higher $R_p$ than NIUMA25. This behavior can be attributed to the shorter $PT$ observed for NIUMA75. In photo-DSC analysis, the time interval ($\Delta_t$) is shorter than in MIR measurements, leading to the $R_p$ being evaluated over a reduced time scale.

The significant discrepancy in monomer conversion values for NIUMAR at 120 s between MIR and photo-DSC analyses can be attributed to differences in sample layer thickness and the distance between the light source and the sample. MIR measurements allow the formation of a thin film and a shorter lamp-to-sample distance (≈2 mm). In contrast, in photo-DSC, the layer thickness cannot be fully controlled, and the lamp is positioned farther from the resin surface (≈10 mm). These conditions can lead to thicker films that exacerbate the negative effects of viscosity and color of NIUMA, and reduced light intensity at the sample, thereby hindering complete monomer conversion. The influence of thickness was confirmed by an additional photo-DSC experiment performed on NIUMAR using 1.39 mg of sample to obtain a thinner film. The resulting curves (Fig. S10) show that both monomer conversion ($C$) and the polymerization rate ($R_p$) increased significantly under these conditions. Although the conversion values were higher than those obtained with a larger sample mass, they remained lower than the MIR results, likely due to the greater lamp-to-sample distance, a parameter that cannot be reduced in photo-DSC experiments.

Although NIUMAR exhibits sufficient reactivity to produce solid materials, as shown in Fig. S11, its high viscosity prevents its application in vat photopolymerization 3D printing. Therefore, the subsequent stages of this work were conducted using only the NIUMA25, NIUMA50, and NIUMA75 resins.

### 3.5. Working curves, 3D printing, and printing resolution study

The resin constants penetration depth ($D_p$) and critical exposure ($E_c$) were determined from Jacobs working curves, shown in Fig. 6a. These parameters are commonly used to evaluate the curing behavior of resins under printing conditions. As shown in Table 5, NIUMA25 exhibited the highest $E_c$ value, whereas NIUMA75 presented the lowest, indicating that the formulation containing the highest NIUMA content requires less energy to reach the gelation point. This behavior of NIUMA75 may be attributed to its higher density of crosslinking points, likely arising from the greater number of reactive sites in NIUMA. This structural feature lowers the energy dose required to reach the gel point, as the crosslink is facilitated [98], consequently reducing the $E_c$ value as the NIUMA content increases in the formulation.

NIUMA75 exhibited the lowest $D_p$ value, followed by NIUMA50 and NIUMA25. The decrease in $D_p$ with increasing NIUMA content is attributed to the darker color of the resin and the effects previously discussed in this work. Notably, all resins analyzed in this study exhibited $E_c$ and $D_p$ values lower than those reported for other renewable formulations based on vegetable oils or methacrylate monomers [62,63,98–102]. Moreover, high $D_p$ values allow photons to penetrate deeper into the resin, which can compromise resolution control and hinder the fabrication of structures with small architectures. Thus, the low $D_p$ values of our resins indicate high printing resolution without the need for photoblockers [63,103].

As all resins demonstrated features for vat photopolymerization 3D printing, two different small and complex-shaped objects (a gyroid and a hexagonal grid) were printed using each formulation and the printing conditions described in Table 2. As can be seen in Fig. 6b, gyroid-shaped objects with a height of 10 mm were successfully 3D-printed and presented high qualitative resolution, as the cavities and the surface of the objects do not present overcuring defects (visually observed) and cracks. The hexagonal grid objects designed with approximately 1 mm thick lines also demonstrated the high accuracy of the NIUMA-based resins, as no overcuring traces are observed. Finally, the different colors observed in the materials arise from the different mass proportions between NIUMA and HEMA in the formulation, in which increasing HEMA content in the formulation seems to result in materials with a less intense brown color.

The printing resolution on the $x/y$-axes of each formulated resin was studied by printing comb-shaped structures (Fig. 6c) containing walls and cavities with different dimensions from a designed CAD model with standard dimensions, as shown in Fig. S12. Because overcuring is the main factor in reducing the printing resolution of photocurable resins, this parameter was evaluated by measuring the dimensions of the 3D-printed models and comparing them with the dimensions of the standard. Furthermore, considering that overcuring decreases the cavity size and increases the lateral size of the rectangles of the comb-shaped structure, the eq. 14 and 15 provided the overcuring percentage in each dimension. Thus, as observed in Fig. 6d and e, and in Table S2, the formulation with the highest amount of HEMA (NIUMA25) presented a percentage of overcuring higher than the others in all dimensions, with the cavity "F" being completely overcured. This result can be associated with the higher $D_p$ presented by this resin. In contrast, NIUMA75 exhibited overall better printing resolution than NIUMA50, which is a direct consequence of its lower $D_p$. These results demonstrate that the renewable and greener resins developed in this work exhibit printing resolutions comparable to, or even better than, those of a non-renewable commercial resin [57].

Although the z-axis resolution was not quantitatively evaluated, the optical microscope images in Fig. 6f show that the 3D-printed gyroid structures from all resins exhibit well-defined and regular layers, indicating good resolution along the $z$-axis. Moreover, the edges of the printed objects are well defined, with no significant cracks or defects observed.

Because high volumetric shrinkage can lead to poor resolution,

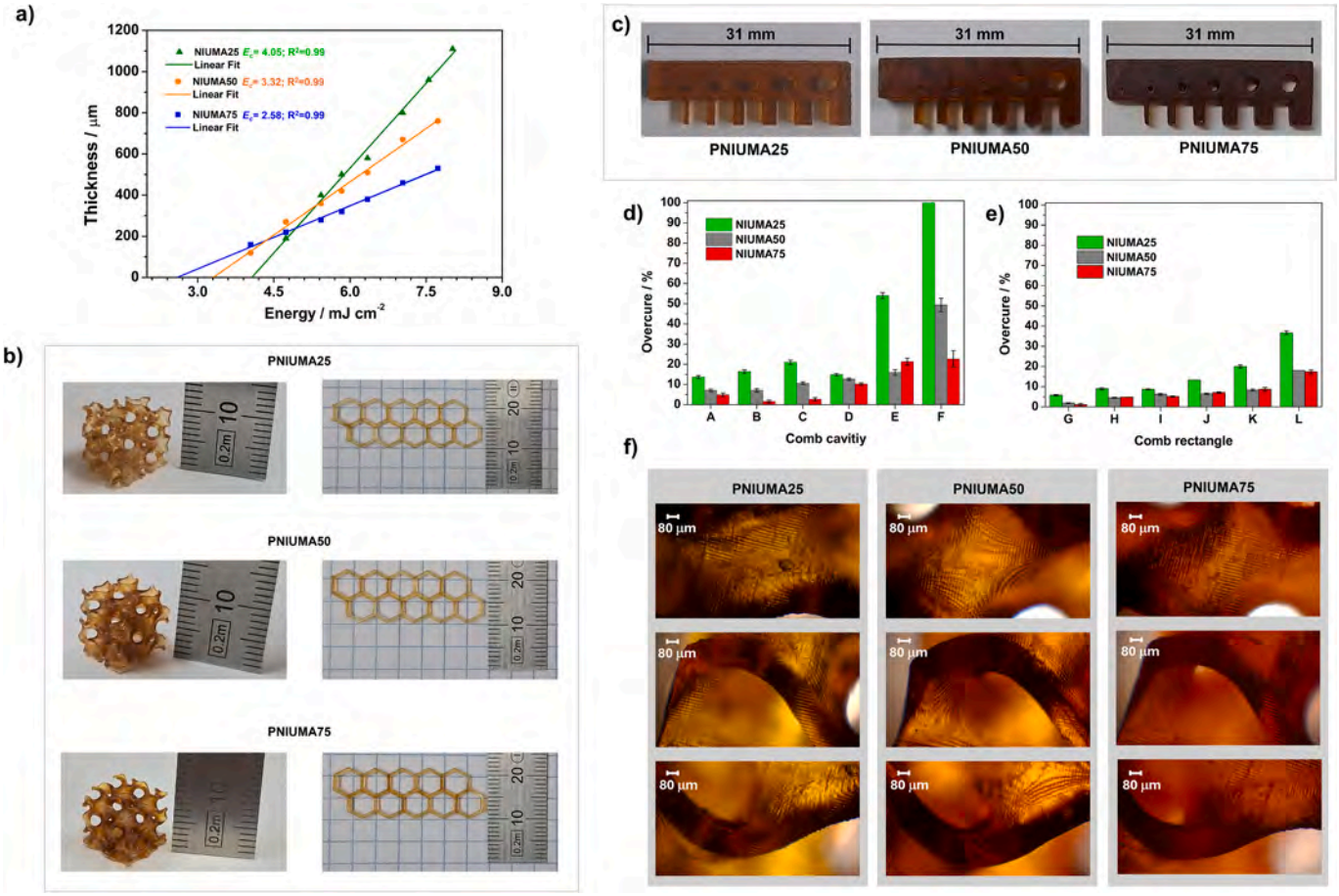


**Fig. 6.** a) Working curves; b) 3D-printed complex-shaped objects; c) 3D-printed comb-shaped test structure for overcuring evaluation; overcuring percentage for d) comb cavities and e) comb rectangles; and f) optical microscopy images of the gyroid object produced from each formulated resin.

microcracks, and residual stresses, thereby compromising the performance of resins in high-resolution 3D printing applications [104], this parameter was evaluated for the NIUMA25, NIUMA50, and NIUMA75 formulations using the density-based method [105]. For this purpose, the average density of each uncured resin and the corresponding 3D-printed material was determined using a pycnometer, with all measurements performed in triplicate.

As shown in Table S3, no significant differences were observed among the densities of the uncured resins. In contrast, increasing the HEMA concentration in the formulations resulted in higher densities for the cured materials. As presented in Table 5, this increase in density after 3D printing produced a larger difference between the uncured and cured states, leading NIUMA25 to exhibit the highest volumetric shrinkage value (6.7 ± 0.1%). This behavior can be attributed to the reduction in free volume promoted by the higher HEMA content in the formulation.

Furthermore, the volumetric shrinkage values obtained for all resins developed in this work were lower than those reported by Ling et al. [106] for methacrylate-based resins. These results indicate that the proposed formulations can be considered low-volumetric-shrinkage resins, highlighting their potential for high-resolution 3D-printing applications.

Overall, the results presented in this section position the NIUMA25, NIUMA50, and NIUMA75 resins at a level comparable to commercial resins, enabling the fabrication of complex-shaped objects with high dimensional accuracy and opening new opportunities for their application in the development of scaffold-like materials with tailored geometries [107,108].

### *3.6. TG/DTG-DTA, DSC, DMA, gel content, hardness, tensiometric analysis, and hydrolysis test*

Thermogravimetric analysis (Fig. 7a) showed that the thermal stability ($T_{stability}$) of the polymers was affected by the amounts of HEMA and NIUMA in the formulation. As shown in Table 6, increasing the NIUMA content increases $T_{stability}$, with PNIUMA75 presenting the highest value (187.0 °C). This enhancement may be attributed to the formation of more densely crosslinked networks, as NIUMA provides multiple crosslinking sites, with an average functionality of 2.55 methacrylic double bonds, as determined by $^1$H NMR spectroscopy. Notably, all polymers developed in this study exhibited higher $T_{stability}$ than a polymer fabricated under identical 3D-printing conditions from a non-renewable commercial resin (Fig. S13 and Table S4), reinforcing the potential of these greener formulations for additive manufacturing.

According to the TG and DTG curves, PNIUMA25 exhibited two mass-loss steps, with the first event associated with the degradation of the polymeric matrix mostly composed of polyHEMA and the second with the decomposition of carbonaceous matter, as these steps are accompanied by exothermic events in the DTA curve. In contrast, PNIUMA50 and PNIUMA75 exhibited three mass-loss steps, with the first step associated with the possible decomposition of the polymeric matrix composed of polyNIUMA chains, considering that in these formulations there is a higher amount of NIUMA than in PNIUMA25. This additional step is related to the exothermic events occurring at 367.0 and 362.0 °C in the DTA curve. The second and third steps are related to the same events observed for PNIUMA25 [28]. All TG/DTG-DTA information is provided in Table S4.

The DSC curves of the polymers are exhibited in Fig. 7b, and they

**Table 5**
Resin constants critical energy ($E_c$), and penetration depth ($D_p$) obtained from working curves, along with the coefficient of determination ($R^2$) of each plot.

| Resin | $E_c$ / mJ cm$^{-2}$ | $D_p$ / μm | $R^2$ | Volume Shrinkage (%) |
|---|---|---|---|---|
| NIUMA25 | 4.05 | 273.68 | 0.99 | 6.7 ± 0.1 |
| NIUMA50 | 3.32 | 173.23 | 0.99 | 4.7 ± 0.2 |
| NIUMA75 | 2.58 | 101.79 | 0.99 | 4.1 ± 0.1 |

present the events observed during the heating stage (-30 to 150 °C). As it is possible to observe in all materials, the baseline change is attributed to the glass transition process, in which the mid-point was considered the glass transition temperature ($T_g$). As shown in Table 6, the $T_g$ decreased with the increase in NIUMA content in the formulation. Therefore, PNIUMA25 presented the highest $T_g$, while PNIUMA75 presented the lowest. These results arise from the structural characteristics of the formulation's components, while HEMA is a small molecule with fewer soft segments, NIUMA is a component rich in long and flexible aliphatic chains, which causes an increase in the free volume and allows an increase in chain mobility, then decreasing the $T_g$ [109–111].

Relaxation curves are shown in Fig. 7c, and the corresponding results are summarized in Table 6. As observed from the tan δ curves, the temperature associated with the α-relaxation decreases with increasing NIUMA content in the formulation, in good agreement with the $T_g$ values obtained from DSC analysis. In addition, a secondary relaxation is observed for PNIUMA25 and PNIUMA50. This behavior may be related to network heterogeneity arising from the different polymerization rates of NIUMAR (PT = 4 s) and HEMA (PT = 7 s), as evidenced by photo-DSC analysis.

The higher reactivity of NIUMAR may promote compositional and topological heterogeneities during curing. As the NIUMAR-rich phase polymerizes and crosslinks more rapidly, HEMA molecules may become preferentially distributed in regions with lower crosslink density, leading to distinct molecular environments within the polymer network. Such heterogeneities can result in multiple relaxation processes detectable by DMA. Similar behavior was reported by Zakrzewski et al. [108] for photocurable resin systems based on pentaerythritol tetraacrylate and the reactive diluent 2-ethylhexyl methacrylate.

The crosslinking density of each 3D-printed polymer was determined using eq. 17. As shown in Table 6, decreasing the HEMA content in the formulation led to an increase in the $\nu$ values. This behavior is attributed to the high functionality of NIUMA, as evidenced by the TG-DTA curves. In contrast, the polymer chains formed from HEMA do not contribute to the crosslinking of the polymer network, since this methacrylate diluent is a monofunctional monomer and therefore does not participate completely in network crosslinking [112].

From the tensile test, the stress-strain curve was obtained for each polymer, as exhibited in Fig. 7d. The summarized results obtained from the curves are shown in Table 6. A clear tendency in the strain is observed. The increase in NIUMA content led to an increase in the strain value, resulting in PNIUMA75 with the highest value (15.0%) and PNIUMA25 with the lowest (4.0%). This behavior can be attributed to the presence of long aliphatic chains in NIUMA (fatty chains), which impart greater chain mobility and flexibility to the polymer network

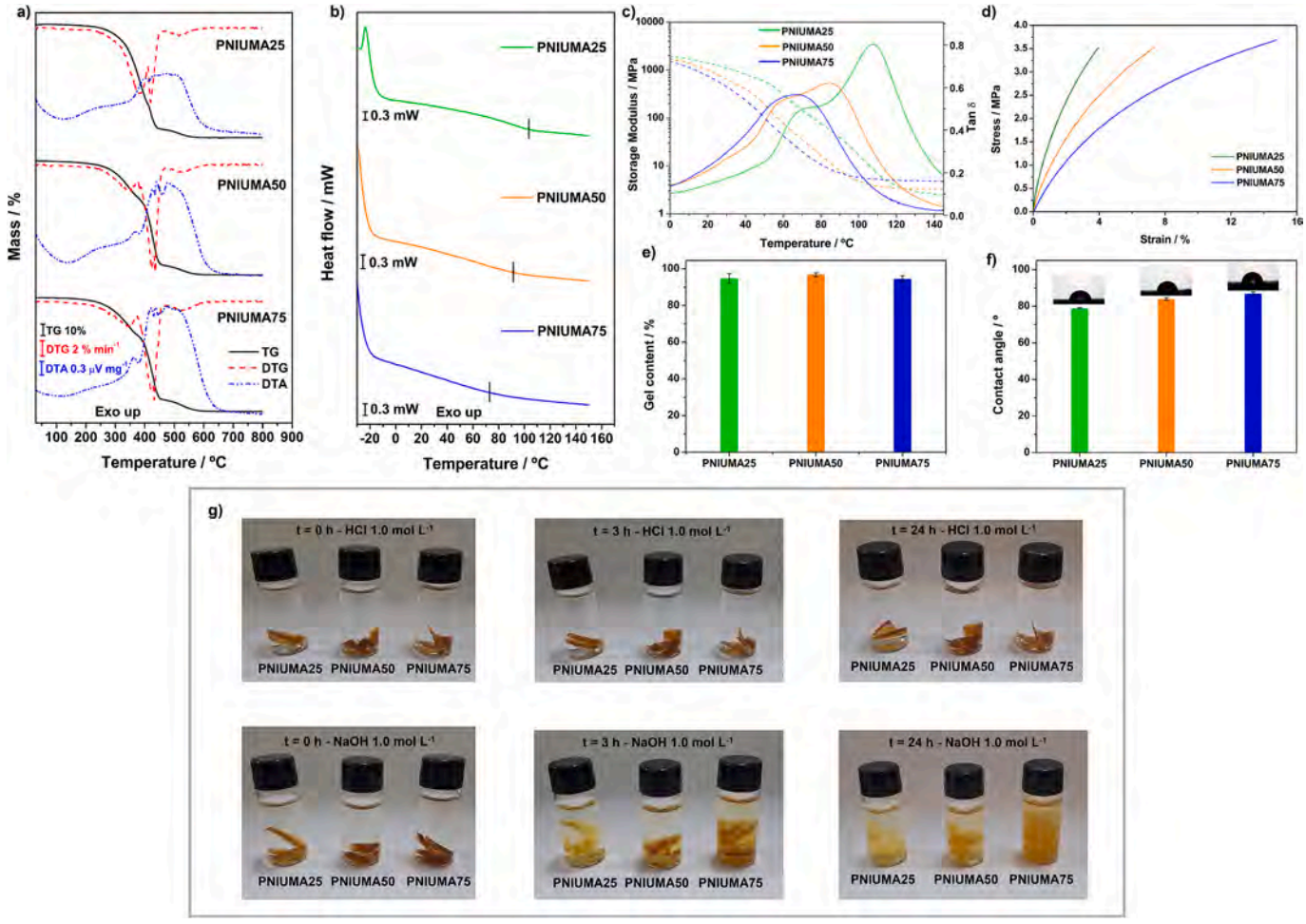


**Fig. 7.** Curves obtained from a) TG/DTG-DTA, b) DSC, c) relaxation, and d) tensile strength analysis for each 3D-printed polymer. Graphs of e) gel content and f) contact angle. g) Pictures at different times (0, 3, and 24 h) of the hydrolysis test.

**Table 6**
Physicochemical properties of each 3D-printed material.

| | PNIUMA25 | PNIUMA50 | PNIUMA75 |
|---|---|---|---|
| $T_{stability}$ / °C | 161.0 | 169.0 | 187.0 |
| $T_g$ / °C | 104.0 | 91.0 | 72.0 |
| Tan δ | 107.4 | 84.3 | 67.0 |
| $\nu$/ mol m$^{-3}$ | 233.6 | 338.2 | 565.0 |
| $E'_g/E'_r$ | 500.0 | 240.0 | 108.0 |
| [a]Strain / % | 4.0[a] | 7.4[a] | 15.0[a] |
| [a]Tensile strength / MPa | 3.5[a] | 3.5[a] | 3.7[a] |
| Young's modulus / MPa | 240.0 ± 2.7 | 130.0 ± 1.6 | 67.0 ± 0.4 |
| *GC* / % | 95.0 ± 3 | 98.0 ± 1 | 95.0 ± 2 |
| Hardness / Shore D | 77.0 ± 0.2 | 66.0 ± 0.2 | 53.0 ± 0.4 |
| Contact angle / ° | 79.0 ± 0.3 | 84.0 ± 0.7 | 87.0 ± 0.8 |

[a] The maximum strain and tensile strength were determined at the point of maximum force, as the samples did not break under the performed experimental conditions.

[113]. Meanwhile, the tensile strength remained relatively constant across all samples, indicating that it is not significantly influenced by NIUMA or HEMA contents. In contrast, the Young's modulus increased with the increase of HEMA in the formulation, resulting in PNIUMA75 with the lowest value, reinforcing its flexible character.

The gel content (*GC*) value is a parameter related to the number of crosslinked chains in a determined polymer network. Therefore, as shown in Fig. 7e and Table 6, the *GC* values of the 3D-printed polymers from all resins are similar, indicating that the materials are highly crosslinked, even using a monofunctional reactive diluent (HEMA).

The hardness value of PNIUMA25, PNIUMA50, and PNIUMA75 was determined and exhibited in Table 6. It is noticeable that increasing the HEMA amount in formulation led to rigid materials, while higher amounts of NIUMA tend to produce soft materials. These results follow the same trend observed in the Young's modulus.

From tensiometric analysis, it is possible to determine the contact angle of materials, which is, in other words, their wettability, since the tests were performed using water [56,114]. Materials with a contact angle $\leq 90°$ are considered hydrophilic, while materials with a contact angle $\geq 90°$ are classified as hydrophobic. As can be seen in Fig. 7f and Table 6, the increase of HEMA in the formulation led to materials with a more hydrophilic character, which can be attributed to its polar characteristics (hydroxyl groups). Meanwhile, the formulation containing the highest amount of NIUMA (PNIUMA75) resulted in materials with a value close to hydrophobic materials, due to the highly apolar character of the aliphatic chains in the triglyceride, which mostly dominate the structure of this monomer.

The hydrolysis test shown in Fig. 7g exhibits the behavior of the 3D-printed materials under acidic and basic conditions. Under acidic conditions, no observable degradation is observed in the materials. On the other hand, in a basic medium, all materials exhibited a certain level of degradation, which varied according to the formulation. For example, after 3 h, PNIUMA25 and PNIUMA50 seem to be less degraded than PNIUMA75. However, after 24 h, all materials appear to have lost integrity, indicating a high level of degradation.

As shown by the results of this section, materials with different chemical and mechanical properties can be obtained depending on the formulation used, demonstrating the versatility of NIUMA for producing materials with properties on demand. Furthermore, although direct comparisons should be made with caution due to differences in testing conditions, a qualitative assessment against literature data (Table S5) indicates that the NIUMA-based materials exhibit higher elongation than those reported for non-isocyanate polyurethane-derived resins. In addition, the elongation, tensile strength, or Young's modulus values obtained in this work can be, in some cases, compared to those reported for materials based on acrylated vegetable oils, acrylated epoxidized vegetable oils formulated with partially renewable reactive diluents, thiol-ene systems, and (meth)acrylated lignin-derived phenolic resins.

### 3.7. Shape memory, luminescence, reprocessing, and self-healing tests

Shape memory polymers (SMPs) are capable of undergoing a reversible change in shape in response to an external stimulus (e.g., heating). Upon stimulation, the material is temporarily deformed and retains this new shape until the stimulus is reapplied, at which point it recovers its original/permanent shape. Materials exhibiting this smart behavior have significant potential for applications in various fields, including functional textiles [115], active aircraft components [116], and adaptive biomedical devices [117].

Initially, the SMP behavior of our polymers was preliminarily determined by analyzing the ratio between storage modulus values at the glassy- and rubbery-state ($E'_g/E'_r$), as already reported by Zhao et al. [105]. According to the authors, a ratio above 100 indicates great potential for SMP behavior, as it results from a dramatic decrease in the modulus with increasing temperature [105]. Similarly to the aforementioned work, we obtained the $E'_g$ value at 25 °C and the $E'_r$ at the plateau of the rubbery state (Tan δ + 40 °C). Therefore, as can be seen in Table 6, all 3D-printed materials demonstrated good potential for SMP behavior, with all modulus ratios above 100. It should be noted that PNIUMA25 presented the highest value, indicating a high-performance SMP material. After this evaluation, complex-shaped 3D-printed objects fabricated from each resin were qualitatively evaluated for SMP behavior. As shown in Fig. 8a, all materials exhibited shape memory properties, although with different recovery times to their permanent shape. Notably, PNIUMA75 showed the fastest recovery, fully returning to its permanent shape within 70 s, which can be attributed to its lower glass transition temperature. In contrast, due to their higher rigidity, materials with higher HEMA contents required longer recovery times, reaching complete recovery after 100 s (PNIUMA25) and 150 s (PNIUMA50). The SMP behavior noticed in all materials is a result of the structural characteristics of NIUMA and HEMA. Based on the phase transition theory [118]. We suggested that the aliphatic chains of NIUMA and the polyHEMA chains (without crosslinking) act as the active phase above the $T_g$, enabling conformational mobility and allowing the storage of internal stress after deformation into a temporary shape, followed by cooling. In contrast, the crosslinked points within the polymer network remain as the frozen phase, serving as physical netpoints that encode the "memory" of the polymer and ensure recovery to its original shape upon reheating.

As exhibited in Fig. 8b, all 3D-printed polymers presented luminescent properties when irradiated with UV light (370 nm). It is suggested that this property is a result of the aggregation-induced emission (AIE) in NIUMA. The AIE effect arises from the clustering of electron-rich atoms, such as oxygen and nitrogen, which promotes orbital overlap and the formation of low-lying LUMO states. In combination with molecular restriction effects, radiative decay pathways are facilitated, resulting in luminescent materials [119,120]. In our case, the functional groups attached to NIUMA make it a strong source of electron-rich atoms, resulting in luminescent materials via the AIE effect. This feature of NIUMA-based polymers is interesting since polymers with the AIE effect have been applied in important fields such as polymeric light-emitting diodes (PLEDs) [121], chemo-biosensing, bioimaging, and photodynamic therapy [122,123].

As described by Chen et al. [124] polyhydroxyurethanes (PHU) can undergo transcarbamoylation exchange reactions due to the presence of urethane and hydroxyl groups in the polymer network. Besides, when vegetable oils are used to produce PHU, transesterification exchange reactions can also occur in the presence of dibutyltin dilaurate (DBTDL) as the catalyst [125,126]. Therefore, the synthetic approach to produce the NIUMA was chosen to produce a monomer containing urethane and ester groups in the triglyceride structure, which can further produce materials with exchangeable covalent bonds and enormous potential for producing DPNs. As a proof-of-concept, we developed a NIUMA75 resin containing 3 wt% DBTDL (named NIUMA75-DB). Since the NIUMA monomer does not present a significant number of free hydroxyls

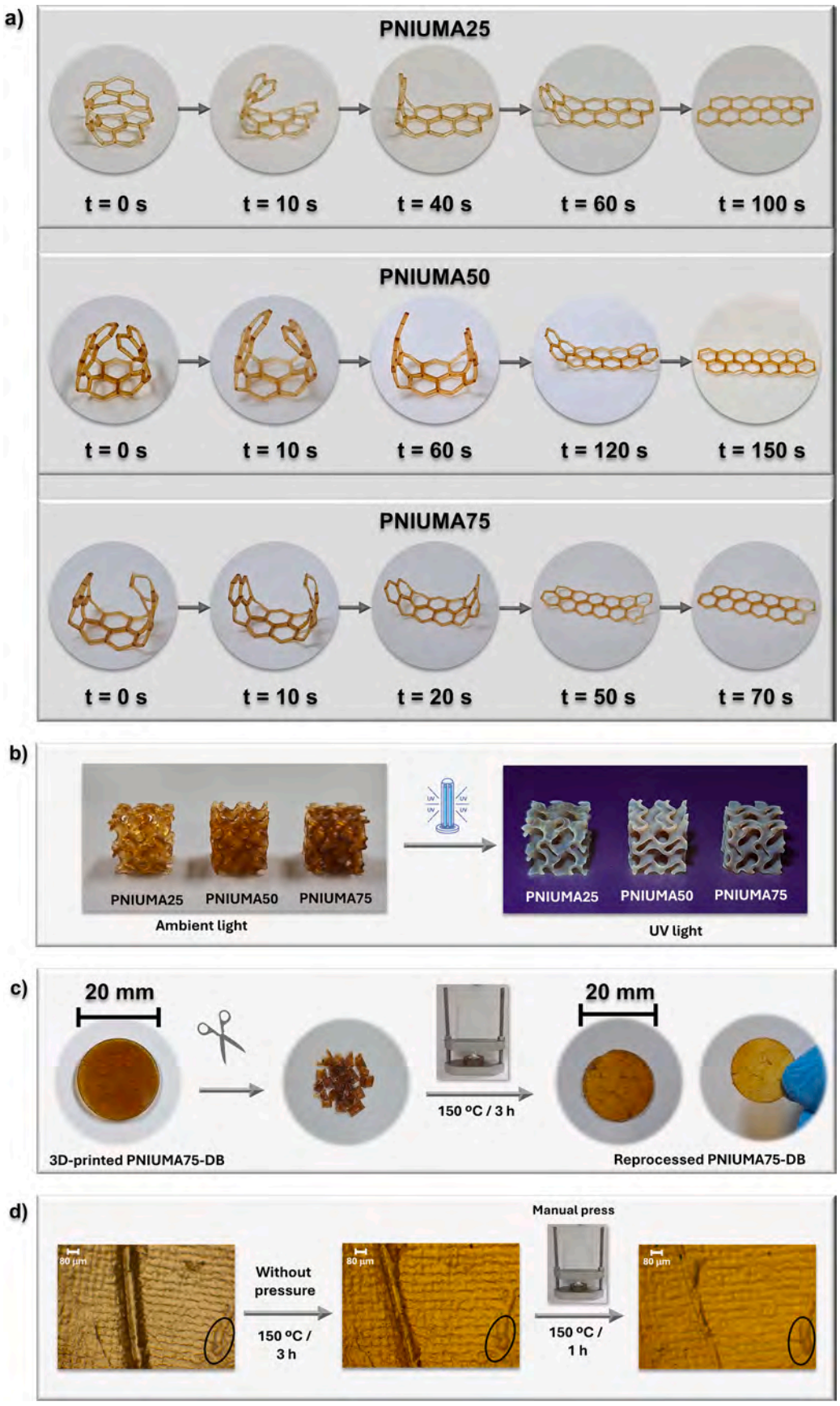


**Fig. 8.** a) Shape memory and b) luminescent behavior of PNIUMA25, PNIUMA50, and PNIUMA75. c) Reprocessing and d) self-healing tests with PNIUMA75-DB.

(secondary alcohol), HEMA was chosen not only as the reactive diluent, but as a source of primary free hydroxyls, which can participate in these exchange reactions. Furthermore, DBTDL was chosen because it has the ability to catalyze transcarbamoylation reactions with both primary and secondary alcohols, as previously verified by Bakkali-Hassani et al. [35] Hence, NIUMA75-DB was used to print a circular form (named as PNIUMA75-DB and shown in Fig. 8c), which was further submitted to a reprocessing test. The reprocessing was performed by cutting the material into small pieces and placing them in a circular-shaped mold. Then, the system was placed in a manual press (Fig. 8c), which was pressed as much as possible. Finally, the system was inserted in an oven at 150 °C for 3 h.

The self-healing test was performed by scratching PNIUMA75-DB in three different places and directions using a razor blade, heating it at 150 °C under no pressure for 3 h, and applying manual pressure (using the manual press) for 1 h.

As shown in Fig. 8c, PNIUMA75-DB presented features for reprocessability, since a defined material could be obtained without compromising its chemical structure, as indicated by its similar thermal stability (184.0 °C) presented after the reprocessing test (Fig. S14 and Table S2). Additionally, the appearance of a new mass-loss step between 85 and 184 °C is attributed to ethanolamine evaporation, which likely occurred due to reversible cyclic carbonate aminolysis exchange reactions. This assumption is supported by comparing the MIR spectra of PNIUMA75-DB collected before and after reprocessing. As shown in Fig. S15, an increase in the intensity of the C═O and C—O bands at 1793 and 1049 $cm^{-1}$, associated with the cyclic carbonate ring, was observed after reprocessing, confirming the occurrence of reversible aminolysis exchange reactions, in agreement with previous reports by Chen et al. [127] In addition, the band at 1653 $cm^{-1}$, observed in the reprocessed PNIUMA75-DB, is attributed to N—H bending of free ethanolamine [71]. To better understand the activation of the dynamic process in PNIUMA75-DB, the material was submitted to 10 min of heating without pressure at different temperatures. After each heating (and cooling to room temperature), a MIR spectrum of the material was collected. As can be seen in Fig. S15c, the intensity of the C═O band from the cyclic carbonate groups does not change until 110 °C. However, after this temperature, its intensity increases, demonstrating the occurrence of the dynamic process of reversible aminolysis exchange.

PNIUMA75-DB also presented healing capabilities. As shown in Fig. 8d and Fig. S16, the microscopic images of PNIUMA75-DB show that the scratches in the material reduced considerably after 3 h of heating without pressure, and it completely healed after 1 h under pressure (a reference point was highlighted with a black circle). The same behavior was observed in the other scratches, as exhibited in Fig. S16. As an initial study, it is possible to suggest that the formulation containing the highest amount of NIUMA exhibited DPN behavior, which will be further studied in subsequent work.

## 4. Conclusions

In this study, a vegetable oil-based non-isocyanate urethane methacrylate monomer (NIUMA) was successfully synthesized and characterized. Novel renewable photocurable resins were subsequently developed by incorporating HEMA as a reactive diluent, effectively overcoming the high viscosity of the pure NIUMA-based formulation. This strategy yielded resins with bio-based carbon content exceeding 40% and SFS values ranging from 21 to 38, highlighting their potential as renewable and sustainable photocurable resins. The curing behavior during photopolymerization of the resins demonstrated that HEMA-containing formulations exhibit high reactivity and are suitable for rapid curing. Additionally, the photolysis study suggested that the structural characteristics of the NIUMA monomer confer UV-absorbing capability, which may promote self-initiation of polymerization when exposed to UV light. This feature was suggested to be responsible for achieving high monomer conversions, as observed in MIR and photo-DSC results. The high reactivity of the photocurable resins enabled their application in vat photopolymerization 3D printing, allowing the fabrication of renewable, complex-shaped objects with high resolution and lower impact from the evaluated overcuring and volume shrinkage. Comprehensive characterization of the 3D-printed materials revealed tunable thermal, mechanical, hardness, and wettability properties as a function of the NIUMA/HEMA ratio, making these materials adaptable for diverse applications or on-demand property optimization. Additionally, all materials underwent degradation under alkaline conditions, mitigating the risk of long-term environmental accumulation. The presence of shape-memory and luminescent properties was qualitatively verified across all materials, further broadening their potential application scope. Finally, in alignment with circular-economy principles, the formulation with the highest NIUMA content and DBDTL as a catalyst was used to print a dynamic polymer network, yielding a material with reprocessing and self-healing capabilities, possibly resulting from transesterification, transcarbamoylation, and reversible cyclic carbonate aminolysis. These results highlight the potential of these renewable formulations for producing materials with high efficiency and developing a greener additive manufacturing. Furthermore, this work opens new opportunities for reprocessable bio-based non-isocyanate urethane methacrylate polymers produced by vat photopolymerization 3D printing.

## CRediT authorship contribution statement

**Gabriel I. dos Santos:** Writing – original draft, Methodology, Investigation, Funding acquisition, Formal analysis, Conceptualization. **Caroline Gaglieri:** Writing – original draft, Methodology, Investigation, Formal analysis. **Rafael T. Alarcon:** Writing – original draft, Methodology, Investigation, Formal analysis. **Marco Sangermano:** Writing – review & editing, Formal analysis, Data curation. **Gilbert Bannach:** Writing – review & editing, Supervision, Project administration, Funding acquisition, Data curation, Conceptualization.

## Declaration of competing interest

The authors declare that they have no known competing financial interests or personal relationships that could have appeared to influence the work reported in this paper.

## Acknowledgments

This study was financed, in part, by the São Paulo Research Foundation (FAPESP), Brazil, process numbers: 2024/14279-1; 2025/19302-4; 2024/00779-2; 2025/02636-7. The authors would like to acknowledge the National Council for Scientific and Technological Development - CNPq (grant 303968/2024-9) for financial support. The authors gratefully acknowledge Professor Éder Tadeu Gomes Cavalheiro for providing access to his laboratory and DMA equipment. The authors acknowledge the Multi-User Equipment Center of the Faculty of Sciences (CEMFC) and FAPESP (Proc. 09/14628-6 and 24/02935-1) for the MIR and UV–Vis analyses.

## Appendix A. Supplementary data

Supplementary data to this article can be found online at https://doi.org/10.1016/j.susmat.2026.e02145.

## Data availability

Data will be made available on request.

## References


[1] S. Amukarimi, Z. Rezvani, N. Eghtesadi, M. Mozafari, Smart biomaterials: from 3D printing to 4D bioprinting, Methods 205 (2022) 191–199, https://doi.org/10.1016/j.ymeth.2022.07.006.

[2] A. Kumar, L.A. Connal, Cationic UV-curing of bio-based epoxidized castor oil vitrimers with electrically conductive properties, React. Funct. Polym. 200 (2024) 105936, https://doi.org/10.1002/marc.202200892.

[3] O. King, M.M. Pérez-Madrigal, E.R. Murphy, A.A.R. Hmayed, A.P. Dove, A. C. Weems, 4D printable salicylic acid photopolymers for sustained drug releasing, shape memory, soft tissue scaffolds, Biomacromolecules 24 (2023) 4680–4694, https://doi.org/10.1021/acs.biomac.3c00416.

[4] S. Nam, D. Mooney, Polymeric tissue adhesives, Chem. Rev. 121 (2021) 11336–11384, https://doi.org/10.1021/acs.chemrev.0c00798.

[5] G. Wu, P. Xie, H. Yang, K. Dang, Y. Xu, M. Sain, L.S. Turng, W. Yang, A review of thermoplastic polymer foams for functional applications, J. Mater. Sci. 56 (2021) 11579–11604, https://doi.org/10.1007/s10853-021-06034-6.

[6] A.D. Valino, J.R.C. Dizon, A.H. Espera, Q. Chen, J. Messman, R.C. Advincula, Advances in 3D printing of thermoplastic polymer composites and nanocomposites, Prog. Polym. Sci. 98 (2019) 101162, https://doi.org/10.1016/j.progpolymsci.2019.101162.

[7] A. Gomez-Lopez, S. Panchireddy, B. Grignard, I. Calvo, C. Jerome, C. Detrembleur, H. Sardon, Poly(hydroxyurethane) adhesives and coatings: state-of-the-art and future directions, ACS Sustain. Chem. Eng. 9 (2021) 9541–9562, https://doi.org/10.1021/acssuschemeng.1c02558.

[8] A.S. Sarala, B.S. Donslund, T. Skrydstrup, Recent advances in the chemical recycling of polyurethane consumer products, Engineering 43 (2025) 5831–5862, https://doi.org/10.1016/j.eng.2025.11.031.

[9] C. Zavarise, J.C. Cintrat, E. Romero, A. Sallustrau, Isocyanate-based multicomponent reactions, RSC Adv. 14 (2024) 39253–39267, https://doi.org/10.1039/d4ra04152f.

[10] J.A.M. Vargas, K.S. Mandrekar, R. Echemendía, A.C.B. Burtoloso, Innovations in isocyanate synthesis for a sustainable future, Org. Biomol. Chem. 23 (2025) 487–505, https://doi.org/10.1039/d4ob01598c.

[11] S. Impemba, D. Bandelli, R. Mastrangelo, G. Poggi, D. Chelazzi, P. Baglioni, Development of biobased poly(urethanes-co-oxazolidones) organogels, Soft Matter 21 (2025) 2623–2632, https://doi.org/10.1039/D5SM00020C.

[12] C. Bakkali-Hassani, D. Berne, V. Ladmiral, S. Caillol, Transcarbamoylation in polyurethanes: underestimated exchange reactions? Macromolecules 55 (2022) 7974–7991, https://doi.org/10.1021/acs.macromol.2c01184.

[13] R.T. Alarcon, C. Gaglieri, G. Bannach, É.T.G. Cavalheiro, Greener preparation of a flexible material based on macaw palm oil derivatives and CO2, Green Chem. 26 (2024) 3261–3270, https://doi.org/10.1039/D3GC03933A.

[14] J. Chen, G. Chiarioni, G.-J.W. Euverink, P.P. Pescarmona, Dyes as efficient and reusable organocatalysts for the synthesis of cyclic carbonates from epoxides and CO2, Green Chem. 25 (2023) 9744–9759, https://doi.org/10.1039/D3GC02161K.

[15] L. Guo, K.J. Lamb, M. North, Recent Developments in Organocatalysed Transformations of Epoxides and Carbon Dioxide Into Cyclic Carbonates 23, 2021, pp. 77–118, https://doi.org/10.1039/D0GC03465G.

[16] J.W. Comerford, I.D.V. Ingram, M. North, X. Wu, Sustainable metal-based catalysts for the synthesis of cyclic carbonates containing five-membered rings, Green Chem. 17 (2015) 1966–1987, https://doi.org/10.1039/c4gc01719f.

[17] M.M. Ramirez-Corredores, Sustainable production of CO2-derived materials, NPJ Mater. Sustain. 2 (2024) 35, https://doi.org/10.1038/s44296-024-00041-9.

[18] A. Gulzar, A. Gulzar, M.B. Ansari, F. He, S. Gai, P. Yang, Carbon dioxide utilization: a paradigm shift with CO2 economy, Chem. Eng. J. Adv. 3 (2020) 100013, https://doi.org/10.1016/j.ceja.2020.100013.

[19] P. Anastas, N. Eghbali, Green chemistry: principles and practice, Chem. Soc. Rev. 39 (2009) 301–312, https://doi.org/10.1039/B918763B.

[20] F.M. Kerton, Applying the principles of green chemistry to achieve a more sustainable polymer life cycle, Curr. Opin. Green Sustain. Chem. 51 (2025) 100996, https://doi.org/10.1016/j.cogsc.2024.100996.

[21] H.N. Cheng, R.A. Gross, P.B. Smith, Green polymer chemistry: pipelines toward new products and processes, ACS Symp. Ser. 1310 (2018) 1–11, https://doi.org/10.1021/bk-2018-1310.ch001.

[22] G. Chyr, J.M. DeSimone, Review of high-performance sustainable polymers in additive manufacturing, Green Chem. 25 (2023) 453–466, https://doi.org/10.1039/D2GC03474C.

[23] A. Ncube, S. Mtetwa, M. Bukhari, G. Fiorentino, R. Passaro, Circular economy and green chemistry: the need for radical innovative approaches in the design for new products, Energies (Basel) 16 (2023) 1752, https://doi.org/10.3390/en16041752.

[24] B.H. Lipshutz, Sachin Handa, modernizing the 12 principles of green chemistry: it's time, Green Chem. (2026), https://doi.org/10.1039/D5GC05289K.

[25] F. Kurul, B. Doruk, S.N. Topkaya, Principles of green chemistry: building a sustainable future, Discov. Chem. 2 (2025) 68, https://doi.org/10.1007/s44371-025-00152-9.

[26] R.T. Alarcon, G.I. dos Santos, C. Gaglieri, A. de Moura, É.T.G. Cavalheiro, G. Bannach, Lipidic biomass as a renewable chemical building block for polymeric materials, Chem. Commun. 60 (2024) 14557–14572, https://doi.org/10.1039/D4CC04993D.

[27] R.V.V. de Lopes, J.R. Zamian, I.S. Resck, M.J.A. Sales, M.L. Dos Santos, F.R. Da Cunha, Physicochemical and rheological properties of passion fruit oil and its polyol, Eur. J. Lipid Sci. Technol. 112 (2010) 1253–1262, https://doi.org/10.1002/ejlt.201000098.

[28] G.I. dos Santos, C. Gaglieri, R.T. Alarcon, R. Magri, M. Hartlieb, G. Bannach, Passion fruit seed oil: a sustainable feedstock for additive manufacturing of renewable polymers, J. Polym. Environ. 32 (2024) 4748–4762, https://doi.org/10.1007/s10924-024-03282-w.

[29] R.T. Alarcon, C. Gaglieri, K.J. Lamb, M. North, G. Bannach, Spectroscopic characterization and thermal behavior of baru nut and macaw palm vegetable oils and their epoxidized derivatives, Ind. Crop. Prod. 154 (2020) 112585, https://doi.org/10.1016/J.INDCROP.2020.112585.

[30] C. Gaglieri, R.T. Alarcon, A. De Moura, R. Magri, L.C. Da Silva-Filho, G. Bannach, Green and efficient modification of grape seed oil to synthesize renewable monomers, J. Braz. Chem. Soc. 32 (2021) 2120–2131, https://doi.org/10.21577/0103-5053.20210104.

[31] R.T. Alarcon, C. Gaglieri, J. de Freitas, G. Bannach, É.T.G. Cavalheiro, Synthesis and characterization of self-healing polymers obtained from polyphenols and cyclic carbonates of amide derivative of macaw palm oil, J. Polym. Environ. 33 (2024) 1159–1170, https://doi.org/10.1007/s10924-024-03479-z.

[32] N. Zheng, Z. Fang, W. Zou, Q. Zhao, T. Xie, Thermoset shape-memory polyurethane with intrinsic plasticity enabled by transcarbamoylation, Angew. Chem. Int. Ed. 128 (2016) 11593–11597, https://doi.org/10.1002/ange.201602847.

[33] W. Alabiso, S. Schlögl, The impact of vitrimers on the industry of the future: chemistry, properties and sustainable forward-looking applications, Polymers (Basel) 12 (2020) 1660, https://doi.org/10.3390/polym12081660.

[34] X. Chen, L. Li, T. Wei, D.C. Venerus, J.M. Torkelson, Reprocessable Polyhydroxyurethane network composites: effect of filler surface functionality on cross-link density recovery and stress relaxation, ACS Appl. Mater. Interfaces 11 (2018) 2398–2407, https://doi.org/10.1021/acsami.8b19100.

[35] C. Bakkali-Hassani, D. Berne, P. Bron, L. Irusta, H. Sardon, V. Ladmiral, S. Caillol, Polyhydroxyurethane covalent adaptable networks: looking for suitable catalysts, Polym. Chem. 14 (2023) 3610–3620, https://doi.org/10.1039/D3PY00579H.

[36] P. Yan, W. Zhao, X. Fu, Z. Liu, W. Kong, C. Zhou, J. Lei, Multifunctional polyurethane-vitrimers completely based on transcarbamoylation of carbamates: thermally-induced dual-shape memory effect and self-welding, RSC Adv. 7 (2017) 26858–26866, https://doi.org/10.1039/C7RA01711A.

[37] C. Gaglieri, R.T. Alarcon, A. de Moura, G. Bannach, Vegetable oils as monomeric and polymeric materials: a graphical review, Curr. Res. Green Sustainable Chem. 5 (2022) 100343, https://doi.org/10.1016/j.crgsc.2022.100343.

[38] Matilde Porcarello, Ettore Greco, R.T. Alberto Cellai, Elizabeth Rossegger Alarcon, Marco Sangermano, 3D printing with biobased epoxidized formulations based on vegetable oils with dynamic polymer network properties, Polym. Chem. (2026), https://doi.org/10.1039/D5PY01069A.

[39] L.T. Nguyen, A. Tharayil, N. Badi, J.M. Winne, F.E. Du Prez, Exploring transamidation and chemical recycling of β-amino amide-derived covalent adaptable networks, Polym. Chem. 16 (2025) 5009–5018, https://doi.org/10.1039/d5py00959f.

[40] M. Sangermano, M. Bergoglio, S. Schögl, Biobased vitrimeric epoxy networks, Macromol. Mater. Eng. 309 (2024) 2300371, https://doi.org/10.1002/mame.202300371.

[41] J. Tu, K. Makarian, N.J. Alvarez, G.R. Palmese, Formulation of a model resin system for benchmarking processing-property relationships in high-performance photo 3D printing applications, Materials 13 (2020) 4109, https://doi.org/10.3390/ma13184109.

[42] L. Pezzana, R. Wolff, J. Stampfl, R. Liska, M. Sangermano, High temperature vat photopolymerization 3D printing of fully bio-based composites: green vegetable oil epoxy matrix & bio-derived filler powder, Addit. Manuf. 79 (2024) 103929, https://doi.org/10.1016/j.addma.2023.103929.

[43] P. Research, 3D Printing Photopolymers Market Size to Hit USD 5.56 Billion by 2035. https://www.precedenceresearch.com/3d-printing-photopolymers-market, 2026 accessed February 6, 2026.

[44] W. Gao, Y. Guo, J. Cui, C. Liang, Z. Lu, S. Feng, Y. Sun, Q. Xia, B. Zhang, Dual-curing polymer systems for photo-curing 3D printing, Addit. Manuf. 85 (2024) 104142, https://doi.org/10.1016/j.addma.2024.104142.

[45] A. Andreu, P.C. Su, J.H. Kim, C. Siang, S. Kim, I. Kim, J. Lee, J. Noh, A. Suriya, Y. J. Yoon, 4D printing materials for vat photopolymerization, Addit. Manuf. 44 (2021) 102024, https://doi.org/10.1016/j.addma.2021.102024.

[46] H.Y. Jeong, S.C. An, Y. Lim, M.J. Jeong, N. Kim, Y.C. Jun, 3D and 4D printing of multistable structures, Appl. Sci. 10 (2020) 1–17, https://doi.org/10.3390/app10207254.

[47] X. Ou, J. Huang, D. Huang, X. Li, G. Chen, Y. Yang, R. Bi, Y. Sheng, S.Z. Guo, 4D-printed snake-like biomimetic soft robots, Bio-Des. Manuf. 8 (2025) 55–67, https://doi.org/10.1631/bdm.2400074.

[48] A. Liguori, E. Oliva, M. Sangermano, M. Hakkarainen, Digital light processing 3D printing of isosorbide- and vanillin-based ester and ester–imine thermosets: structure–property recyclability relationships, ACS Sustain. Chem. Eng. 11 (2023) 14601–14613, https://doi.org/10.1021/acssuschemeng.3c04362.

[49] C. Liu, J. Wen, G. Ma, Z. Wu, J. Qu, Bio-based UV-curable non-isocyanate urethane-functional acrylates coating with enhanced anti-smudge and anti-graffiti performance, Chem. Eng. J. 521 (2025) 166543, https://doi.org/10.1016/J.CEJ.2025.166543.

[50] N. Singh, H. Bakhshi, W. Meyer, Developing non-isocyanate urethane-methacrylate photo-monomers for 3D printing application, RSC Adv. 10 (2020) 44103–44110, https://doi.org/10.1039/D0RA06388F.

[51] R. Carmenini, C. Spanu, E. Locatelli, L. Sambri, M. Comes Franchini, M. Maturi, Isocyanate-free urethanediol itaconates as biobased liquid monomers in photopolymerization-based 3D printing, Prog. Addit. Manuf. 9 (2024) 2499–2510, https://doi.org/10.1007/s40964-024-00598-w.

[52] C. Liu, D. Liufu, D. Cai, G. Ma, Z. Wu, J. Qu, Synthesis and application of UV-curable non-isocyanate urethane-functional acrylates for coatings and 3D printing, ACS Appl. Polym. Mater. 7 (2025) 7079–7090, https://doi.org/10.1021/acsapm.5c00593.
[53] K.Y. Lam, C.S. Lee, M.R. Pichika, S.F. Cheng, R.Y.H. Tan, Non-isocyanate polyurethane-acrylate as UV- and thermo-responsive plasticizer for thermoplastic elastomer, J. Appl. Polym. Sci. 141 (2024) e55703, https://doi.org/10.1002/APP.55703;WGROUP:STRING:PUBLICATION.
[54] R.T. Alarcon, K.J. Lamb, É.T.G. Cavalheiro, M. North, G. Bannach, A screening process for carbonation of vegetable oils using an aluminum(salen) complex with a further application as weldable polymers, J. Appl. Polym. Sci. 140 (2023) e53962, https://doi.org/10.1002/APP.53962;ISSUE:ISSUE:DOI.
[55] D. Prat, A. Wells, J. Hayler, H. Sneddon, C.R. McElroy, S. Abou-Shehada, P. J. Dunn, CHEM21 selection guide of classical- and less classical-solvents, Green Chem. 18 (2016) 288–296, https://doi.org/10.1039/C5GC01008J.
[56] R.T. Alarcon, A. Cellai, M. Porcarello, B. Sölle, E. Rossegger, C.C. Schmitt, M. Sangermano, Green design of renewable dual-curing polymers with self-healing and recyclable networks for 3D printing, ACS Sustain. Chem. Eng. 13 (2025) 16136–16153, https://doi.org/10.1021/acssuschemeng.5c07154.
[57] G.I. dos Santos, C. Gaglieri, R.T. Alarcon, A. de Moura, F.B. dos Santos, G. Bannach, Glycerol and maleic anhydride-based acrylic polyester: a solution for greener photocurable resins for 3D printing of renewable materials, ACS Sustain. Chem. Eng. 13 (2025) 9771–9782, https://doi.org/10.1021/ACSSUSCHEMENG.5C03006.
[58] A.B. Kousaalya, B. Ayalew, S. Pilla, Photopolymerization of acrylated epoxidized soybean oil: a photocalorimetry-based kinetic study, ACS Omega 4 (2019) 21799–21808, https://doi.org/10.1021/ACSOMEGA.9B02680.
[59] G. Colucci, F. Di Stefano, F. Sacchi, M. Licciardello, C. Tonda-Turo, L. Lavagna, M. Messori, Bio-based polymer composites obtained by vat photopolymerization of photocurable resins modified with biochar as sustainable filler, Compos. Part A Appl. Sci. Manuf. 198 (2025) 109102, https://doi.org/10.1016/J.COMPOSITESA.2025.109102.
[60] D.S. Esen, F. Karasu, N. Arsu, The investigation of photoinitiated polymerization of multifunctional acrylates with TX-BT by photo-DSC and RT-FTIR, Prog. Org. Coat. 70 (2011) 102–107, https://doi.org/10.1016/J.PORGCOAT.2010.10.010.
[61] M. Maturi, E. Locatelli, A. Sanz de Leon, M. Comes Franchini, S.I. Molina, Sustainable approaches in vat photopolymerization: advancements, limitations, and future opportunities, Green Chem. 27 (2025) 8710–8754, https://doi.org/10.1039/D5GC02299A.
[62] R.P. Rosa, G. Rosace, R. Arrigo, G. Malucelli, Preparation and characterization of a fully biobased resin system for 3d-printing, suitable for replacing fossil-based acrylates, J. Polym. Res. 30 (2023) 139, https://doi.org/10.1007/S10965-023-03523-X.
[63] G. Zhu, J. Zhang, J. Huang, X. Yu, J. Cheng, Q. Shang, Y. Hu, C. Liu, L. Hu, Y. Zhou, High-performance 3D printing UV-curable resins derived from soybean oil and gallic acid, Green Chem. 23 (2021) 5911–5923, https://doi.org/10.1039/d1gc01934a.
[64] L.M. Stevens, E.A. Recker, K.A. Zhou, V.G. Garcia, K.S. Mason, C. Tagnon, N. Abdelaziz, Z.A. Page, Counting all photons: efficient optimization of visible light 3D printing, Adv. Mater. Technol. 8 (2023) 2300052, https://doi.org/10.1002/ADMT.202300052.
[65] L. Ballester-Bayarri, A. Pascal, J. Ayestaran, A. Gonzalez, N. Ballard, R. Aguirresarobe, 3D printing of vinylogous urethane-based methacrylic covalent adaptable networks by vat photopolymerization, ACS Appl. Polym. Mater. 6 (2024) 2594–2603, https://doi.org/10.1021/ACSAPM.3C02777.
[66] J. Dong, B. Liu, H. Ding, J. Shi, N. Liu, B. Dai, I. Kim, Bio-based healable non-isocyanate polyurethanes driven by the cooperation of disulfide and hydrogen bonds, Polym. Chem. 11 (2020) 7524–7532, https://doi.org/10.1039/D0PY01249A.
[67] X. Liu, X. Yang, S. Wang, S. Wang, Z. Wang, S. Liu, X. Xu, H. Liu, Z. Song, Fully bio-based Polyhydroxyurethanes with a dynamic network from a terpene derivative and cyclic carbonate functional soybean oil, ACS Sustain. Chem. Eng. 9 (2021) 4175–4184, https://doi.org/10.1021/ACSSUSCHEMENG.1C00033.
[68] N. Fanjul-Mosteirín, L.P. Fonseca, A.P. Dove, H. Sardon, Bio-based non-isocyanate poly(hydroxy urethane)s (PHU) derived from vanillin and CO2, Mater. Adv. 4 (2023) 2437–2448, https://doi.org/10.1039/D3MA00111C.
[69] S. El Khezraji, M. Chaib, S. Thakur, M. Raihane, M.A. Lopez-Manchado, R. Verdejo, M. Lahcini, Synthesis of novel non-isocyanate polyurethane/functionalized boron nitride composites, Polymers (Basel) 14 (2022) 3934, https://doi.org/10.3390/polym14193934.
[70] G. Seychal, C. Ocando, L. Bonnaud, J. De Winter, B. Grignard, C. Detrembleur, H. Sardon, N. Aramburu, J.M. Raquez, Emerging polyhydroxyurethanes as sustainable thermosets: a structure–property relationship, ACS Appl. Polym. Mater. 5 (2023) 5567–5581, https://doi.org/10.1021/ACSAPM.3C00879.
[71] D.L. Pavia, G.M. Lampman, G.S. Kriz, J.R. Vyvyan, Infrared spectroscopy, in: D. L. Pavia, G.M. Lampman, G.S. Kriz, J.R. Vyvyan (Eds.), Introduction to Spectroscopy, 5th ed, Cengage Learning, 2014, pp. 15–126.
[72] Z. Ling, L. Gu, Q. Zhou, UV-curable hybrid NIPU for coating and 3D printing applications, ACS Appl. Polym. Mater. 7 (2025) 7884–7892, https://doi.org/10.1021/ACSAPM.5C00818.
[73] F. Zareanshahraki, H.R. Asemani, J. Skuza, V. Mannari, Synthesis of non-isocyanate polyurethanes and their application in radiation-curable aerospace coatings, Prog. Org. Coat. 138 (2020) 105394, https://doi.org/10.1016/J.PORGCOAT.2019.105394.
[74] J.M. Marchetti, A.F. Errazu, Comparison of different heterogeneous catalysts and different alcohols for the esterification reaction of oleic acid, Fuel 87 (2008) 3477–3480, https://doi.org/10.1016/J.FUEL.2008.05.011.
[75] H. Fouilloux, W. Qiang, C. Robert, V. Placet, C.M. Thomas, Multicatalytic transformation of (meth)acrylic acids: a one-pot approach to biobased poly(meth) acrylates, Angew. Chem. Int. Ed. 60 (2021) 19374–19382, https://doi.org/10.1002/ANIE.202106640;WGROUP:STRING:PUBLICATION.
[76] J. Guit, M.B.L. Tavares, J. Hul, C. Ye, K. Loos, J. Jager, R. Folkersma, V.S.D. Voet, Photopolymer resins with biobased Methacrylates based on soybean oil for stereolithography, ACS Appl. Polym. Mater. 2 (2020) 949–957, https://doi.org/10.1021/ACSAPM.9B01143.
[77] P. Zhang, J. Xin, J. Zhang, Effects of catalyst type and reaction parameters on one-step acrylation of soybean oil, ACS Sustain. Chem. Eng. 2 (2013) 181–187, https://doi.org/10.1021/SC400206T.
[78] THE 17 GOALS | Sustainable Development. https://sdgs.un.org/goals, 2026 accessed January 1, 2026.
[79] J.P. Montheard, M. Chatzopoulos, D. Chappard, 2-hydroxyethyl methacrylate (hema): chemical properties and applications in biomedical fields, J. Macromol. Sci. Part C Polym. Rev. 32 (1992) 1–33, https://doi.org/10.1080/15321799208018377.
[80] O. Rosales-Calderon, V. Arantes, A review on commercial-scale high-value products that can be produced alongside cellulosic ethanol, Biotechnol. Biofuels 12 (2019) 240, https://doi.org/10.1186/S13068-019-1529-1/FIGURES/6.
[81] J.S. Terry, A.C. Taylor, The properties and suitability of commercial bio-based epoxies for use in fiber-reinforced composites, J. Appl. Polym. Sci. 138 (2021) 50417, https://doi.org/10.1002/APP.50417;REQUESTEDJOURNAL:JOURNAL:10974628;PAGE:STRING:ARTICLE/CHAPTER.
[82] J. Dai, S. Ma, Y. Wu, J. Zhu, X. Liu, High bio-based content waterborne UV-curable coatings with excellent adhesion and flexibility, Prog. Org. Coat. 87 (2015) 197–203, https://doi.org/10.1016/J.PORGCOAT.2015.05.030.
[83] F.K. Adom, J.B. Dunn, Life cycle analysis of corn-Stover-derived polymer-grade l-lactic acid and ethyl lactate: greenhouse gas emissions and fossil energy consumption, Biofuels Bioprod. Biorefin. 11 (2017) 258–268, https://doi.org/10.1002/BBB.1734;WEBSITE:WEBSITE:SCIJOURNALS;PAGE:STRING:ARTICLE/CHAPTER.
[84] J.T. Miao, S. Peng, M. Ge, Y. Li, J. Zhong, Z. Weng, L. Wu, L. Zheng, Three-dimensional printing fully biobased heat-resistant photoactive acrylates from aliphatic biomass, ACS Sustain. Chem. Eng. 8 (2020) 9415–9424, https://doi.org/10.1021/ACSSUSCHEMENG.0C02168.
[85] V. Schimpf, A. Asmacher, A. Fuchs, B. Bruchmann, R. Mülhaupt, Polyfunctional acrylic non-isocyanate hydroxyurethanes as photocurable thermosets for 3D printing, Macromolecules 52 (2019) 3288–3297, https://doi.org/10.1021/ACS.MACROMOL.9B00330.
[86] M. Lebedevaite, V. Talacka, J. Ostrauskaite, High biorenewable content acrylate photocurable resins for DLP 3D printing, J. Appl. Polym. Sci. 138 (2021) 50233, https://doi.org/10.1002/APP.50233;WGROUP:STRING:PUBLICATION.
[87] A. Jagtap, A. More, A review on self-initiated and photoinitiator-free system for photopolymerization, Polym. Bull. 79 (2021) 8057–8091, https://doi.org/10.1007/S00289-021-03887-4.
[88] T. Scherzer, W. Knolle, S. Naumov, R. Mehnert, Direct initiation of the photopolymerization of acrylates by short-wavelength excimer UV radiation, Nucl. Inst. Methods Phys. Res. B 208 (2003) 271–276, https://doi.org/10.1016/S0168-583X(03)00620-7.
[89] W. Yan, J. de la Vega, Ö. Eroğlu, L. Heisenberg, D. Wang, High power sunlight-simulated UV-induced radical polymerization: self-initiation and self-crosslinking, Macromol. Mater. Eng. 309 (2024) 2300456, https://doi.org/10.1002/MAME.202300456;JOURNAL:JOURNAL:15229505;REQUESTEDJOURNAL:JOURNAL:14392054;WGROUP:STRING:PUBLICATION.
[90] R.T. Alarcon, C. Gaglieri, K.J. Lamb, É.T.G. Cavalheiro, M. North, G. Bannach, A new acrylated monomer from macaw vegetable oil that polymerizes without external photoinitiators, J. Polym. Res. 28 (2021) 425, https://doi.org/10.1007/s10965-021-02787-5.
[91] J. Feng, D. Ye, Self-photoinitiating water-diluted polyurethane acrylates and their UV-curing kinetics, Prog. Org. Coat. 129 (2019) 300–308, https://doi.org/10.1016/J.PORGCOAT.2019.01.027.
[92] M. Lebedevaite, J. Ostrauskaite, E. Skliutas, M. Malinauskas, Photoinitiator free resins composed of plant-derived monomers for the optical μ-3D printing of thermosets, Polymers 11 (2019) 116, https://doi.org/10.3390/POLYM11010116.
[93] J.S. Young, A.R. Kannurpatti, C.N. Bowman, Effect of comonomer concentration and functionality on photopolymerization rates, mechanical properties and heterogeneity of the polymer, Macromol. Chem. Phys. 199 (1998) 1043–1049, https://doi.org/10.1002/(SICI)1521-3935(19980601)199 (6).
[94] M. Par, P. Burrer, K. Prskalo, S. Schmid, A.L. Schubiger, D. Marovic, Z. Tarle, T. Attin, T.T. Tauböck, Polymerization kinetics and development of polymerization shrinkage stress in rapid high-intensity light-curing, Polymers (Basel) 14 (2022) 3296, https://doi.org/10.3390/POLYM14163296.
[95] S.H. Dickens, J.W. Stansbury, K.M. Choi, C.J.E. Floyd, Photopolymerization kinetics of methacrylate dental resins, Macromolecules 36 (2003) 6043–6053, https://doi.org/10.1021/MA021675K.
[96] P. Garra, C. Dietlin, F. Morlet-Savary, F. Dumur, D. Gigmes, J.P. Fouassier, J. Lalevée, Photopolymerization processes of thick films and in shadow areas: a review for the access to composites, Polym. Chem. 8 (2017) 7088–7101, https://doi.org/10.1039/C7PY01778B.
[97] O.C. Dorterler, F. Yilmaz, O. Tokul Olmez, Color-dependent polymerization: the impact of curing time on the conversion degree and microhardness of colored

compomers, Polymers (Basel) 17 (2025) 2155, https://doi.org/10.3390/POLYM17152155.
[98] C. Vazquez-Martel, L. Becker, W.V. Liebig, P. Elsner, E. Blasco, Vegetable oils as sustainable inks for additive manufacturing: a comparative study, ACS Sustain. Chem. Eng. 9 (2021) 16840–16848, https://doi.org/10.1021/ACSSUSCHEMENG.1C06784.
[99] M. Bodor, A. Lasagabáster-Latorre, G. Arias-Ferreiro, M.S. Dopico-García, M. J. Abad, Improving the 3D printability and mechanical performance of biorenewable soybean oil-based photocurable resins, Polymers (Basel) 16 (2024) 977, https://doi.org/10.3390/POLYM16070977.
[100] J. Yao, M. Karlsson, M. Lawoko, K. Odelius, M. Hakkarainen, Microwave-assisted organosolv extraction for more native-like lignin and its application as a property-enhancing filler in a light processable biobased resin, RSC Sustain. 1 (2023) 1211–1222, https://doi.org/10.1039/D3SU00115F.
[101] S. Krishnamoorthy, S. Wadnap, B. Noorani, H. Xu, C. Xu, Investigation of gelatin methacrylate working curves in dynamic optical projection stereolithography of vascular-like constructs, Eur. Polym. J. 124 (2020) 109487, https://doi.org/10.1016/J.EURPOLYMJ.2020.109487.
[102] A.W. Bassett, A.E. Honnig, C.M. Breyta, I.C. Dunn, J.J. La Scala, J.F. Stanzione, Vanillin-based resin for additive manufacturing, ACS Sustain. Chem. Eng. 8 (2020) 5626–5635, https://doi.org/10.1021/ACSSUSCHEMENG.0C00159.
[103] S. Peng, Y. Li, L. Wu, J. Zhong, Z. Weng, L. Zheng, Z. Yang, J.T. Miao, 3D printing mechanically robust and transparent polyurethane elastomers for stretchable electronic sensors, ACS Appl. Mater. Interfaces 12 (2020) 6479–6488, https://doi.org/10.1021/ACSAMI.9B20631/SUPPL_FILE/AM9B20631_SI_003.MP4.
[104] Q. Zhang, S. Weng, C.M. Hamel, S.M. Montgomery, J. Wu, X. Kuang, K. Zhou, H. J. Qi, Design for the reduction of volume shrinkage-induced distortion in digital light processing 3D printing, Extreme Mech. Lett. 48 (2021) 101403, https://doi.org/10.1016/j.eml.2021.101403.
[105] L. Zhao, R. Yu, Y. He, M. Zhang, F. Tian, L. Wang, Y. Zhao, W. Huang, 3D printed epoxy/acrylate hybrid polymers with excellent mechanical and shape memory properties via UV and thermal cationic dual-curing mechanism, Addit. Manuf. 79 (2024) 103904, https://doi.org/10.1016/j.addma.2023.103904.
[106] L. Ling, T. Lai, P.T. Chung, S. Sabet, V. Tran, R. Malyala, A novel 3D-printing model resin with low volumetric shrinkage and high accuracy, Polymers (Basel) 17 (2025) 610, https://doi.org/10.3390/polym17050610.
[107] M. Bergoglio, M. Kriehuber, B. Sölle, E. Rossegger, S. Schlögl, Z. Najmi, A. Cochis, F. Ferla, M. Miola, E. Vernè, M. Sangermano, 3D-printed acrylated soybean oil scaffolds with vitrimeric properties reinforced by tellurium-doped bioactive glass, Polymers (Basel) 16 (2024) 3614, https://doi.org/10.3390/POLYM16243614.
[108] M. Bergoglio, M. Miola, E. Vernè, M. Sangermano, N.R. Cameron, 3D-printed biobased porous polymer scaffolds reinforced with bioactive glasses by high internal phase emulsion polymerization, Biomacromolecules 26 (2025) 8548–8559, https://doi.org/10.1021/ACS.BIOMAC.5C01413.
[109] W. Wang, Z. Hu, W. Lei, Research progress on vegetable oil-based UV-curing resins, Polymers (Basel) 17 (2025) 1890, https://doi.org/10.3390/POLYM17141890.
[110] S. Ghosh, S. Ghosh, Vegetable oil-derived functional polymers in biomedical applications: hurdles and possibilities, J. Mater. Chem. B 13 (2025) 4994–5022, https://doi.org/10.1039/D4TB02648A.
[111] M. Gobin, P. Loulergue, J.L. Audic, L. Lemiègre, Synthesis and characterisation of bio-based polyester materials from vegetable oil and short to long chain dicarboxylic acids, Ind. Crop. Prod. 70 (2015) 213–220, https://doi.org/10.1016/J.INDCROP.2015.03.041.
[112] P. Fässler, B. Grob, I. Lamparth, S. Omeragic, K. Rist, L. Vidal, J. Lalevée, Y. Catel, Evaluation of various monofunctional monomers for the development of fracture tough dental materials exhibiting a low crosslink density, Eur. Polym. J. 219 (2024) 113332, https://doi.org/10.1016/j.eurpolymj.2024.113332.
[113] M. Liu, J. Wang, Q. Yan, J. Lyu, Y. Lei, S. Lyu, L. Yan, Green bio-derived epoxidized linseed-oil plasticizer improves the toughness, strength, and dimensional stability of furfuryl alcohol-modified wood, Ind. Crop. Prod. 217 (2024) 118886, https://doi.org/10.1016/j.indcrop.2024.118886.
[114] T.M. Abbas, S.I. Hussein, Improving the mechanical properties, roughness, thermal stability, and contact angle of the acrylic polymer by graphene and carbon Fiber doping for waterproof coatings, J. Inorg. Organomet. Polym. 32 (2022) 3788–3796, https://doi.org/10.1007/s10904-022-02384-z.
[115] R. Purwar, R. Sachan, Thermoresponsive shape memory polymers for smart textiles, in: S.U. Islam, B.S. Butola (Eds.), Advances in Functional and Protective Textiles, 1st ed, Woodhead Publishing, Amsterdam, 2020, pp. 37–62, https://doi.org/10.1016/B978-0-12-820257-9.00003-5.
[116] A. Yadav, S.K. Singh, S. Das, S. Kumar, A. Kumar, Shape memory polymer and composites for space applications: a review, Polym. Compos. 46 (2025) 11647–11683, https://doi.org/10.1002/pc.29707.
[117] Y.J. Li, F.H. Zhang, Y.J. Liu, J.S. Leng, 4D printed shape memory polymers and their structures for biomedical applications, Sci. China Technol. Sci. 63 (2020) 545–560, https://doi.org/10.1007/s11431-019-1494-0.
[118] Y. Xia, Y. He, F. Zhang, Y. Liu, J. Leng, Y. Xia, Y. He, F. Zhang, J. Leng, Y. Liu, A review of shape memory polymers and composites: mechanisms, materials, and applications, Adv. Mater. 33 (2021) 2000713, https://doi.org/10.1002/adma.202000713.
[119] Z. Zhao, H. Zhang, J.W.Y. Lam, B.Z. Tang, Aggregation-induced emission: new vistas at the aggregate level, Angew. Chem. Int. Ed. 59 (2020) 9888–9907, https://doi.org/10.1002/anie.201916729.
[120] R.T. Alarcon, C. Gaglieri, G.C. dos Santos, A.C. Moralles, N.H. Morgon, A.R. de Souza, G. Bannach, AIE effect by oxygen clustering in vegetable oil-based polymers, ChemistrySelect 6 (2021) 7838–7844, https://doi.org/10.1002/slct.202100889.
[121] J. Gu, Z. Xu, D. Ma, A. Qin, B.Z. Tang, Aggregation-induced emission polymers for high performance PLEDs with low efficiency roll-off, Mater. Chem. Front. 4 (2020) 1206–1211, https://doi.org/10.1039/D0QM00012D.
[122] R. Hu, X. Yang, A. Qin, B.Z. Tang, AIE polymers in sensing, imaging and theranostic applications, Mater. Chem. Front. 5 (2021) 4073–4088, https://doi.org/10.1039/d1qm00078k.
[123] W. Du, X. Liu, L. Liu, J.W.Y. Lam, B.Z. Tang, Photoresponsive polymers with aggregation-induced emission, ACS Appl. Polym. Mater. 3 (2021) 2290–2309, https://doi.org/10.1021/acsapm.1c00182.
[124] X. Chen, L. Li, T. Wei, J.M. Torkelson, Reprocessable polymer networks designed with hydroxyurethane dynamic cross-links: effect of backbone structure on network morphology, phase segregation, and property recovery, Macromol. Chem. Phys. 220 (2019) 1900083, https://doi.org/10.1002/macp.201900083.
[125] S. Hu, X. Chen, J.M. Torkelson, Biobased reprocessable polyhydroxyurethane networks: full recovery of crosslink density with three concurrent dynamic chemistries, ACS Sustain. Chem. Eng. 7 (2019) 10025–10034, https://doi.org/10.1021/acssuschemeng.9b01239.
[126] W. Liu, D.F. Schmidt, E. Reynaud, Catalyst selection, creep, and stress relaxation in high-performance epoxy vitrimers, Ind. Eng. Chem. Res. 56 (2017) 2667–2672, https://doi.org/10.1021/acs.iecr.6b03829.
[127] X. Chen, L. Li, K. Jin, J.M. Torkelson, Reprocessable polyhydroxyurethane networks exhibiting full property recovery and concurrent associative and dissociative dynamic chemistry via transcarbamoylation and reversible cyclic carbonate aminolysis, Polym. Chem. 4 (2017) 6349–6355, https://doi.org/10.1039/C7PY01160A.